THERMAL CHARACTERIZATION OF A HALL EFFECT THRUSTER

THESIS

Alex M. Bohnert, Civilian, USAF

AFIT/GA/ENY/08-M01

DEPARTMENT OF THE AIR FORCE
AIR UNIVERSITY

AIR FORCE INSTITUTE OF TECHNOLOGY

Wright-Patterson Air Force Base, Ohio

AFIT/GA/ENY/08-M01

THERMAL CHARACTERIZATION OF A HALL EFFECT THRUSTER

THESIS

Presented to the Faculty

Department of Aeronautics and Astronautics

Graduate School of Engineering and Management

Air Force Institute of Technology

Air University

Air Education and Training Command

In Partial Fulfillment of the Requirements for the

Degree of Master of Science in Astronautical Engineering

Alex M. Bohnert, BS

Civilian, USAF

March 2008

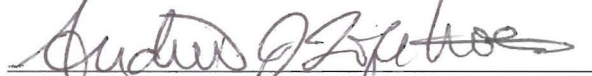APPROVED FOR PUBLIC RELEASE; DISTRIBUTION UNLIMITED

AFIT/GA/ENY/08-M01

THERMAL CHARACTERIZATION OF A HALL EFFECT THRUSTER

Alex M. Bohnert, BS

Civilian, USAF

Approved:

_____
Richard D. Branam, Maj, USAF (Chairman)

_____
Andrew J. Lofthouse, Maj, USAF (Member)

_____
Dr. William Hargus (Member)

7 Mar 08
Date

13 Mar 08
Date

6 Mar 08
Date

Acknowledgments

Table of Contents

List of Figures

List of Tables

Nomenclature

T	= Thrust or Temperature
$\dot{m}$	= Mass Flow
u_e	= Exit Velocity
I_{sp}	= Specific Impulse
g_o	= Sea Level Gravitational Constant
I	= Total Impulse
t	= time
Δv	= Change in Velocity
m_o	= Initial Mass
m_f	= Final Mass
m_{power}	= Power Supply Mass
α	= Specific Power Supply Mass
η	= Electrical to Thrust Power Conversion Efficiency
Δm	= Change in Propellant Mass
F_m	= Electromagnetic Force
j	= Electric Current Density
B	= Magnetic Induction Field
e^-	= Electron
Xe	= Xenon
μm	= Micrometer
mm	= Millimeter
$E_{\lambda,b}$	= Blackbody Radiant Emittance at wavelength λ
λ	= Wavelength
c_o	= Speed of Light
h	= Planck's Constant
k	= Boltzmann's Constant
σ	= Stefan-Boltzmann's Constant
E_b	= Total Blackbody Emissive Power
ε	= Emissivity
E	= Emissive Power
α_λ	= Power Absorbed at Wavelength λ
ρ_λ	= Power Reflected at Wavelength λ
τ_λ	= Power Transmitted at Wavelength λ
τ	= Transmissivity
F	= View Factor
A	= Area
θ	= Angle
R	= Distance

J   = Radiosity
q   = Heat Transfer Rate
W   = Radiated Power
U   = Voltage
C   = Proportionality Constant
slope   = Slope of Camera Correction Trendline
intercept = y Intercept of Camera Correction Trendline
R^2 = Coefficient of determination
x_i = x coordinate of data point
y_i = y coordinate of data point
$\bar{x}$ = Average of x coordinate data
$\bar{y}$ = Average of y coordinate data
n = Number of samples.

AFIT/GA/ENY/08-M01

Abstract

The thermal characteristics of a Hall thruster directly influence thruster and spacecraft design. High temperatures affect the magnetic coil capabilities and cause higher insulator erosion rates, influencing both thruster performance and lifetime. The Hall thruster transfers heat through both radiation and conduction, and the spacecraft must handle this additional thermal energy. An infrared camera provides a non-intrusive method to analyze the thermal characteristics of an operational Hall thruster.

This thesis contains the thermal analysis of a Busek Co. Inc. 200 W Hall thruster, using a FLIR ThermaCAM SC640 infrared camera. The Space Propulsion Analysis and System Simulator Laboratory at the Air Force Institute of Technology on Wright-Patterson Air Force Base provided the location for thruster set up and operation. The infrared camera furnishes the surface temperatures for the entire thruster, and approximates the transient heating behavior during start up, steady state, and shut down. Thermocouples verify and correct the camera data. Experimentally determined emissivities characterize the materials of the thruster. In addition, a view factor analysis between the camera pixels and the alumina sprayed portion of the cathode determines the exchange of radiation between the pixels and cathode surface. This process develops a technique to map surface temperatures of complex geometries with confidence in the actual values. Accurately mapping the surface temperatures of a Hall Effect thruster will improve both thruster efficiency and lifetime, and predict the thruster's thermal load on a satellite.

THERMAL CHARACTERIZATION OF A HALL EFFECT THRUSTER

I. Introduction

A Hall thruster is an electromagnetic propulsion device. These types of devices use interactions of internal and external magnetic fields with electric currents to accelerate an ionized propellant stream.[1] A picture of a Hall thruster can be seen in Figure 1.
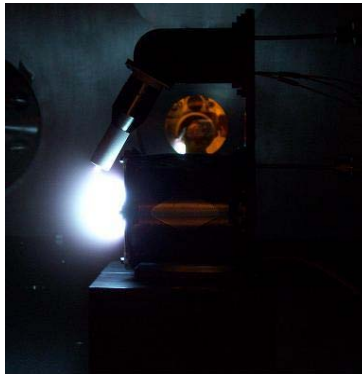
Figure 1. Picture of Hall Thruster in Operation

Hall thruster research began in the 1950s and 1960s in the United States and the Soviet Union. The Russians developed and flew dozens of Hall thrusters on satellites for various functions.[2] The European Space Agency's SMART-1 spacecraft, launched in 2003, used a Hall Thruster as its primary propulsion system as it traveled to and orbited the moon.[3] The United States Air Force Space Vehicles Directorate developed a Hall thruster for TacSat-2, which launched in December 2006.[4] The growing popularity of these devices is due to the thruster's unique characteristics.

Unlike chemical propulsion devices, electromagnetic propulsion systems are not limited by the amount of energy released from a chemical reaction. Instead, they are limited by the ability to apply electromagnetic forces at desired total power levels.[5]

Electric propulsion devices require a separate electrical energy source. For space applications, high specific impulse devices must be tempered by considerations of the power plant weight needed to drive these engines.[1] The following table compares the specific impulse of several types of propulsion systems.

Table 1: Comparison of Space Thruster Values[5]

Type	Specific Impulse (seconds)
Chemical	200-465
Nuclear (thermal)	750-1500
Electrothermal	300-1500
Electromagnetic	1000-10,000
Electrostatic	2000-100,000+

Hall thrusters generally operate at a specific impulse in the range of 1200 to 3000 seconds.[2] Due to weight penalties associated with the electrical power supply, optimal specific impulse for orbital maneuvers is between 1200 and 2000 seconds, which is in the ideal range for Hall thrusters.

The temperature and thermal behavior of the thruster is an important issue. High temperatures can affect the operation of the magnets and cause high erosion rates within the thruster itself. Increasing a magnet temperature causes a decrease in magnetism. The Curie temperature, or Curie point, is the temperature where magnetism becomes zero due to the randomization of the aligned dipoles being disturbed by thermal random motion.[6] At high temperatures, the emission of electrons from the cathode can decrease. These all cause a decrease in thruster efficiency.

Thermometers and thermocouples are commonly used for temperature measurement; however, infrared thermal sensors are becoming less expensive and more reliable.[7] These types of instruments allow a passive and non-intrusive method to measure surface temperatures and thermal distributions. There are several advantages of non-contact thermal infrared (IR) measurements over contact measurements. Non-contact methods are non-intrusive, remote, and much faster than conventional methods; and they measure the temperature at the surface of the object of interest and not the surrounding air.[7] This method does not affect the operation of the thruster, but has its own limitations such as emissivity approximations and roughness of a material's surface. It can also produce a thermal map of an entire surface rather than a point-to-point traditional temperature measurement device.

The purpose of this work is to characterize the thermal behavior of a Hall Effect thruster operating in a vacuum by using a thermal imager to collect radiation data. This information can impact thruster performance and be used to improve thruster and spacecraft design. Hall thrusters are gaining popularity in spacecraft designs because of their large exit velocities and specific impulse. The goals of this research are to experimentally determine the emissivities for all the materials of a Hall Effect thruster, to set up and operate a Hall Effect thruster, and to develop an accurate, passive technique to measure surface temperatures of complex geometries with confidence in the actual temperature values.

This thesis is organized as follows. Chapter 2 will discuss the theory and background of Hall Effect thruster and radiative heat transfer. It will also describe how temperature affects the thruster's operation, and how an infrared camera measures a

3

surfaces' temperature. The emissivity tests and experimental methodology will be covered in Chapter 3. Chapter 4 will explain the temperature mapping technique validated with thermocouples, and the analysis of the radiation exchange between the alumina plasma sprayed stainless steel section of the cathode and the camera pixels. The conclusions reached through this research and recommendations for future research will be expressed in Chapter 5.

II. Background

Chapter Overview

The purpose of this chapter is to describe the missions for a Hall thruster, to describe how it operates and to show how temperature can affect the thruster performance. This chapter also explains radiation heat transfer effects and how a thermal imager works. Some references to similar research and examples of thermal imaging principles being used in other fields is also covered.

Mission Analysis

The mission decides the propulsion system requirements, specifically the thrust, specific impulse, and the propellant mass. Electrical propulsion devices can greatly reduce propellant mass consumption because a greater amount of energy can be added to a given amount of mass.[8] The thrust of a rocket is given by the following equation

$$T = \dot{m}u_e \tag{1}$$

where T is the thrust, $\dot{m}$ rate of change of mass flow, and u_e is the effective exhaust velocity. The specific impulse, $I_{sp,}$ is defined as

$$I_{sp} = \frac{u_e}{g_o} \tag{2}$$

where g_o is the sea-level gravitational acceleration. Specific impulse is a common characteristic parameter of propulsion devices. The total impulse is defined as

$$I = \int_{t_o}^{t_f} T dt \tag{3}$$

where t is time. For missions requiring a large impulse, the desired thrust could be achieved by increasing the exit velocity and not the mass flow rate.[1] The change in velocity of the spacecraft is given by the following equation

$$\Delta v = u_e \ln \frac{m_o}{m_f}$$

(4)

where m_o is the initial mass and m_f is the final mass. The following table shows some typical velocity change requirements for space propulsion.

Table 2: Typical Functions and Requirements for Space Propulsion[2]

Propulsion Function	Typical Requirement (meters/second)
Orbit transfer to geosynchronous orbit	
Perigee burn	2400
Apogee burn	1500-1800
Low earth orbit to higher orbit raising	60-1500
Drag makeup	60-500
Controlled-reentry	120-150
Acceleration to escape velocity from low earth parking orbit	3600-4000
Orbit maintenance	
Orbit correction	15-75 per year
East-West stationkeeping	3-6 per year
North-South stationkeeping	45-55 per year
Survivability or evasive maneuvers	150-4600

Rearranging Equation (4) yields the relation between mass fraction and exit velocity for a given velocity change.

$$\frac{m_f}{m_o} = e^{-\Delta v / u_e}$$

(5)

Equation (5) defines the propellant mass required for each mission. An exit velocity comparable to the velocity change increment will give a greater fraction of the original mass to the final velocity.[1] Hall thrusters are advantageous for these large velocity

change missions such as deep space missions or orbit changes. They also provide a small enough thrust that can be used in orbit correction maneuvers. Figure 2 illustrates the approximate regions of application of different propulsion systems. Hall thrusters provide enough specific impulse for geostationary stationkeeping, solar power orbit transfer, and orbit maneuvering. The lager specific impulse of the Hall thruster translates into a longer operational life for satellites whose life is propellant limited.[9] They also require less operating power than arc jets.
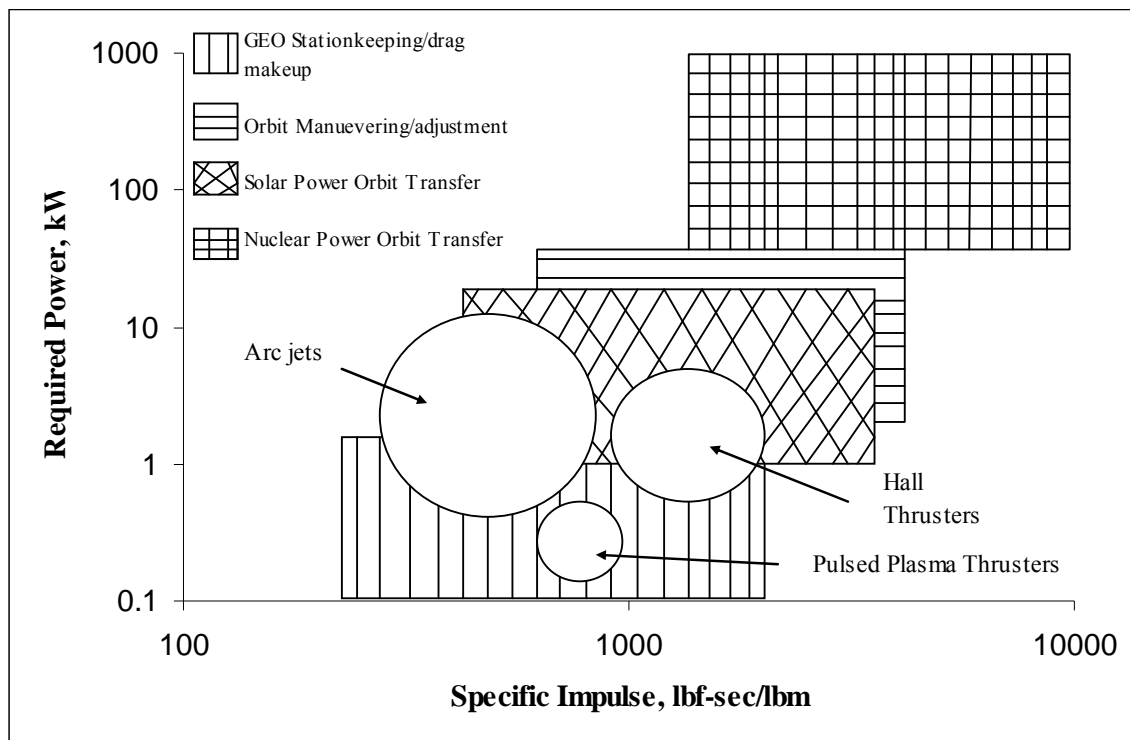
Figure 2. Electric Propulsion Systems Applications[9]

Electric propulsion devices produce high exit velocities, but higher exit velocities require a greater mass of the power supply for constant thrust missions. The mass of the power supply scales directly with exit velocity.[1] Equation (6) shows the relationship between the mass of the power supply and exit velocity

$$m_{power} = \frac{\alpha \dot{m} u_e^2}{2\eta} \qquad (6)$$

where m_{power} is the mass of the power supply, α is the specific power plant mass and η is the conversion efficiency of electrical to thrust power. Figure 3 displays the dependence of propellant mass, Δm, and power supply mass on specific impulse for a constant thrust mission.
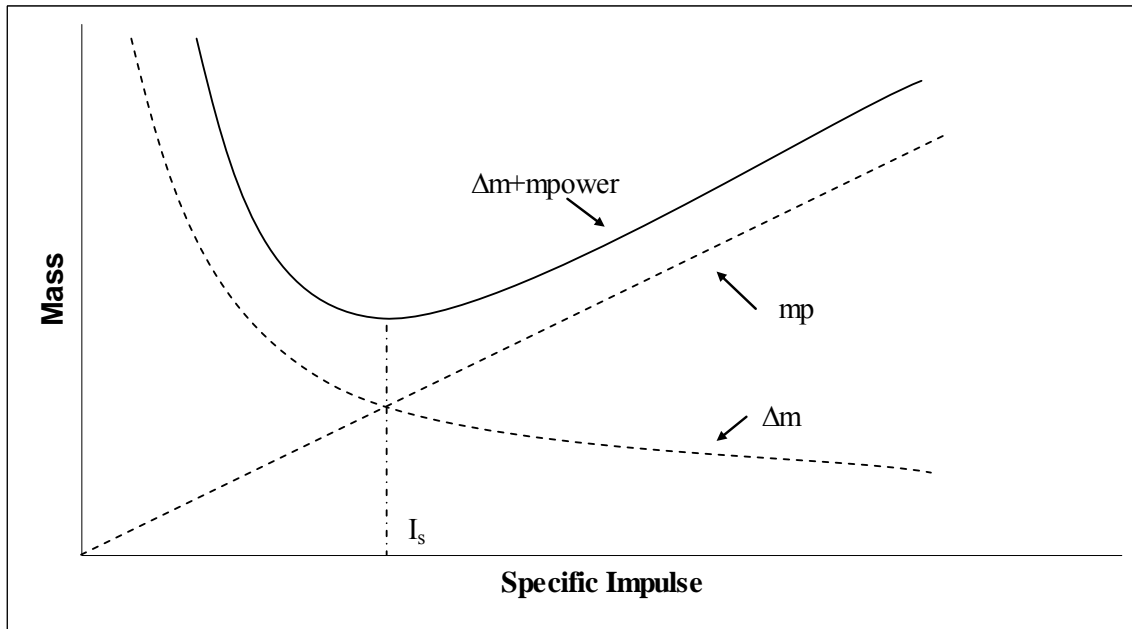
Figure 3. Propellant Mass and Power Supply Mass Dependence on Specific Impulse[1]

It can be seen that tradeoffs between exit velocity and power supply mass produce an optimum specific impulse. This specific impulse will minimize the mass needed to be launched to support the propulsion system.

When compared to chemical propulsion systems, electric propulsion systems, like the Hall thruster, deliver more payload to orbit on orbit transfers. The increased payload capacity gives several benefits, one of which is the increase of useful payload to orbit. Additional fuel would increase the life of the satellite, or additional hardware could

improve satellite capability. The increased payload capacity could also create increased

flexibility in satellite design and possibly even decrease launch vehicle size.[10]

Hall Thruster Operation

Electromagnetic forces provide the acceleration of the propellant flow.[5] Equation

(7) describes the electromagnetic force acting in a Hall thruster.

$$\vec{F}_m = \vec{j} \times \vec{B} \tag{7}$$

F_m is the electromagnetic force per unit volume of gas, j is the electric current density

passing through the gas, and B is the magnetic induction field in the gas. The

electromagnetic force creates higher exit velocities than those of conventional

combustion rockets. Hall thruster operation begins with the generation of electrons by

the cathode. The cathode location is downstream of the thruster. The schematic of a Hall

thruster can be seen in Figure 4.
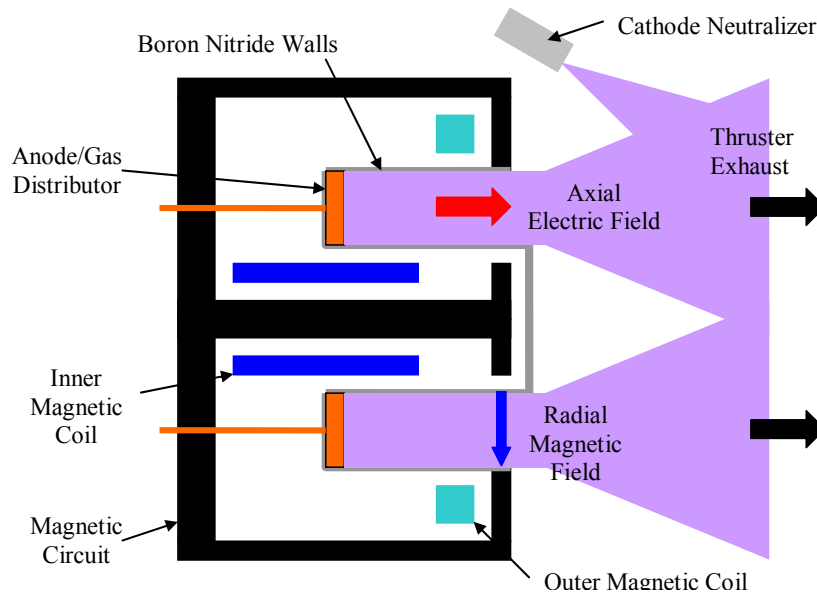
Figure 4. Schematic of Hall Thruster[11]

The anode attracts the electrons and causes them to accelerate into the thruster chamber. As the electrons move toward the anode channel, the high strength magnetic field traps them. The applied magnetic field forces the current to flow in spiral paths along, known as the Hall Effect or Hall current.[5] The current flows in the direction of the electric field crossed with the magnetic field. Hall thrusters generally use an inert gas, such as xenon, mercury, for propellant.[12] Other propellants include mercury and other liquid metals. Some of the electrons collide with the propellant atoms to create ions. Equation (8) illustrates the ionization process with xenon as the propellant.[12]

$$e^- + Xe \rightarrow Xe^+ + 2e^- \tag{8}$$

Xe is xenon, *e* is electron and *+/-* is the charge. This process generates plasma within the thruster chamber, creating interactions between electric and magnetic fields. The electric field between the anode and the circulating electrons accelerate the ions out of the thruster. Some of the electrons emitted from the cathode neutralize the positively charged ions at the thruster exit.

Radiation

All objects at a nonzero temperature emit radiation, allowing for the measurement of temperature. Radiation heat transfer can take place in a vacuum and translates at the speed of light. It occurs by electromagnetic emission and absorption.[7] Radiative heat transfer takes place between wavelengths of 0.75 micrometers and 100 micrometers, which is in the infrared portion of the electromagnetic spectrum. Region 4 in Figure 5 designates the infrared region of the electromagnetic spectrum.
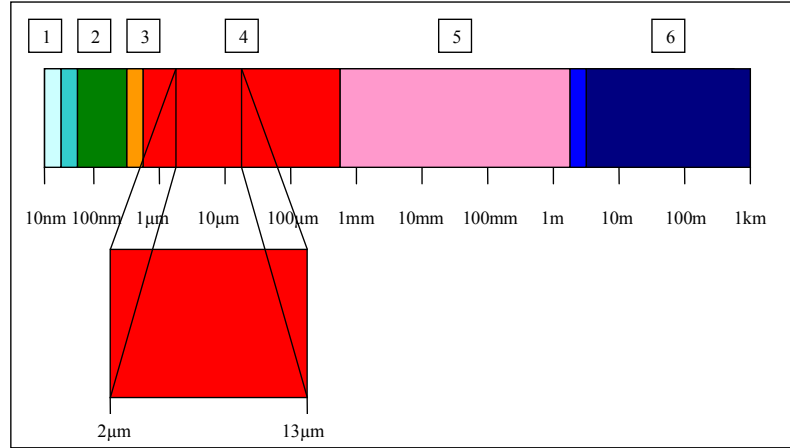
Figure 5. The Electromagnetic Spectrum[18]

A blackbody is the best possible absorber and emitter of radiant energy, regardless of wavelength or direction.[13] Radiation emitted by a blackbody is a function of wavelength and temperature, but it is assumed independent of direction.[14] Blackbody radiation is ideal radiation, and does not represent a real surface. The following equation is the blackbody spectral emissive power.

$$E_{\lambda,b}(\lambda,T) = \frac{2\pi h c_o^2}{\lambda^5 [\exp(h c_o / \lambda k T) - 1]} \qquad (9)$$

$E_{\lambda,b}$ is the blackbody radiant emittance at wavelength λ. T is the absolute temperature, c_o is the speed of light (2.998 X 10^8 meters per second), h is Planck's constant (6.626 X 10^{-34} Joule second) and k is Boltzmann's constant (1.381 X 10^{-23} Joule per Kelvin). Integrating Equation (9) over all wavelengths, leads to the Stefan-Boltzmann Law for the total blackbody emissive power.

$$E_b = \int_0^\infty \frac{2\pi h c_o^2}{\lambda^5 [\exp(h c_o / \lambda k T) - 1]} d\lambda = \sigma T^4 \qquad (10)$$

σ is the Stefan-Boltzmann constant (5.67 X 10^{-8} Watts per meter squared Kelvin).

Equation (10) proves blackbody radiation is proportional to temperature to the fourth power.

Real surfaces are not ideal and use blackbody properties as a reference to describe them. A real surface's spectral and directional distribution differs from a blackbody. Figure 6 displays these differences, forming a basis for the comparison of real surfaces to blackbodies.
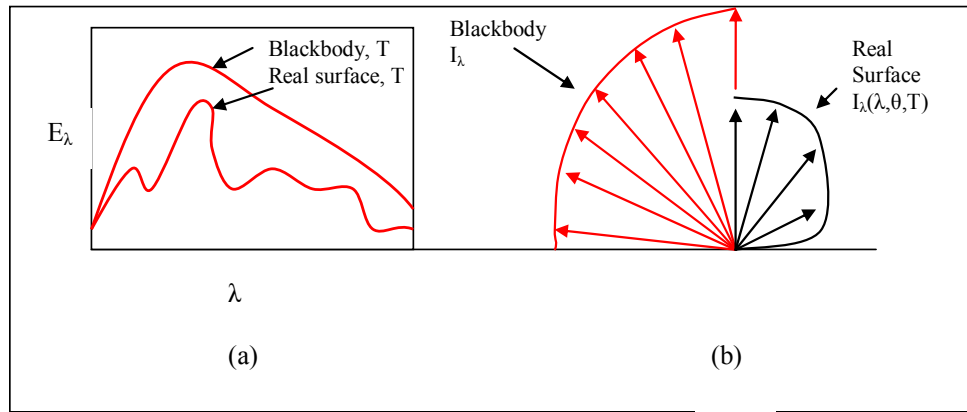
Figure 6. Comparison of Real and Blackbody (a) Spectral and (b) Directional Distribution[14]

A real surface also emits less energy than a blackbody at the same absolute temperature. It has an emissive power given by

$$E = \varepsilon \sigma T^4 \tag{11}$$

where ε is the emissivity. Emissivity is the ratio of the radiation emitted by a surface to the radiation emitted by a blackbody at the same temperature. It is a function of temperature, wavelength, direction and material.[14] Figure 7 shows the wavelength dependence of emissivity of a few materials. The emissivity of a surface is highly dependent on wavelength, and may assume different values depending on the emission at

a given wavelength, or in integrated averages across several wavelengths.[14] This

dependence affects the temperature of the surface.
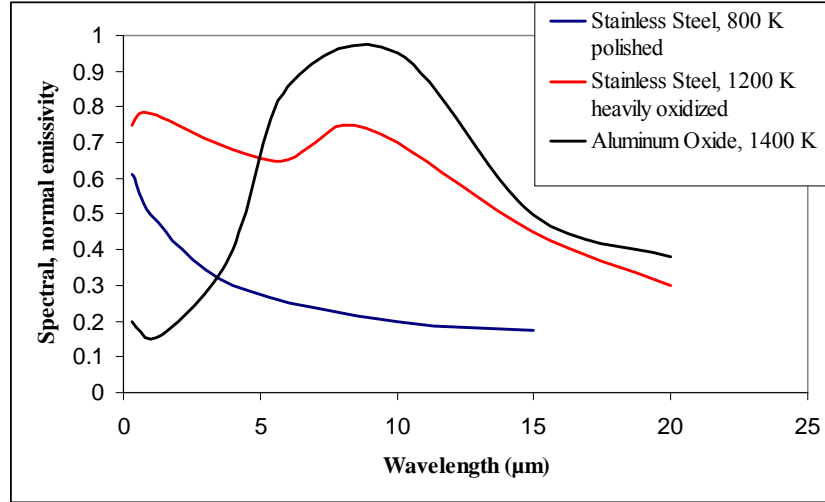
Figure 7. Wavelength Dependence of Emissivity[14]

The following equation is the total, directional emissivity.

$$\varepsilon(T) = \frac{E(T)}{E_b(T)} \tag{12}$$

It represents an average over all possible directions and wavelengths.

Because of the conservation of energy, radiation must be transmitted, reflected or

absorbed by a surface.[15] At any given wavelength, absorptivity, reflectivity, and

transmissivity sum to one, yielding the following equation.

$$\alpha_\lambda + \rho_\lambda + \tau_\lambda = 1 \tag{13}$$

α is the ratio of spectral radiant power absorbed to incident power, ρ is the ratio of

reflected power to incident power and τ is the ratio of transmitted power to incident

power. Kirchhoff's Law states the emissivity of a surface is equal to the absorptivity.

$$\alpha_\lambda = \varepsilon_\lambda \tag{14}$$

13

View factors help compute radiation exchange between any two surfaces. They are also known as the configuration, shape or angle factor. Figure 8 represents two surfaces oriented at an angle to one another. Radiation leaves surface i and is intercepted by surface j. These areas, vectors, and angles develop an expression for the view factor.
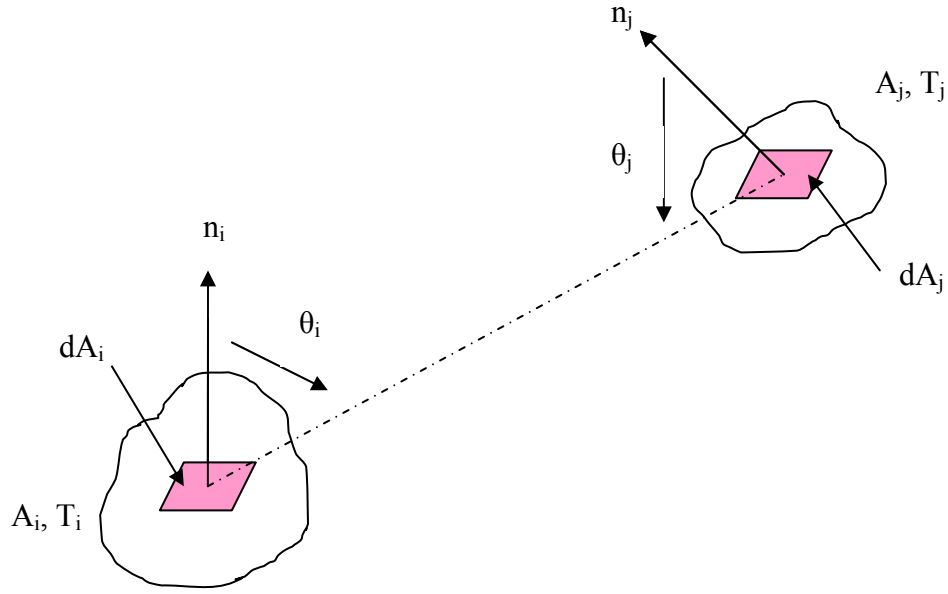
Figure 8. View Factor Associated With Radiation between Two Surfaces[14]

Equation (15) defines the view factor.[16]

$$F_{ij} = \frac{\textit{diffuse energy leaving } A_i \textit{ directly towards and intercepted by } A_j}{\textit{total diffuse energy leaving } A_i} \qquad (15)$$

The view factor can be described mathematically by a double surface integral.

$$F_{ij} = \frac{1}{A_i} \int_{A_i} \int_{A_j} \frac{\cos\theta_i \cos\theta_j}{\pi R^2} dA_i dA_j \qquad (16)$$

F_{ij} is the view factor, R is the distance between areas A_i and A_j, and θ_i and θ_j are the angles between R and the local surface normal.[16] The reciprocity relation helps to determine one view factor by knowing the other.

14

$$A_i F_{ij} = A_j F_{ji} \tag{17}$$

View factors also follow a summation rule.

$$\sum_{j=1}^{N} F_{ij} = 1 \tag{18}$$

Radiosity (J_i) takes into account both radiation emitted and reflected from a surface. Analyzing radiation exchanges between two surfaces is made easier with a few assumptions. Each surface is assumed isothermal and characterized by a uniform radiosity and irradiation. The medium is taken as nonparticipating and diffuse, gray surface behavior should be assumed.[14] Equation (19) expresses the net radiative heat transfer rate from a surface.

$$q_i = \frac{E_{bi} - J_i}{(1 - \varepsilon_i)/\varepsilon_i A_i} \tag{19}$$

E_{bi} is the blackbody emissive power of surface I, q_i is the net radiative heat transfer rate from a surface, J_i is the radiosity, ε_i is the emissivity, and A_i is the area. The irradiation of a surface is calculated from the radiosities of other surfaces. It can be found by the following equation.

$$q_i = \sum_{j=1}^{N} A_i F_{ij} (J_i - J_j) = \sum_{j=1}^{N} q_{ij} \tag{20}$$

Combining Equation (19) and Equation (20) yields the following equation.

$$\frac{E_{bi} - J_i}{(1 - \varepsilon_i)/\varepsilon_i A_i} = \sum_{j=1}^{N} A_i F_{ij} (J_i - J_j) \tag{21}$$

A direct approach for solving radiation problems can be found by writing out Equation (21) for each surface. Solving a matrix of these equations produces J_i for each surface. With the radiosities of each surface known, Equation (19) may be used to determine the

net radiation heat transfer rate.[14] From each q_i, Equation (11) can be used to calculate the temperature of each surface.

Infrared Camera Measurement

Infrared cameras receive radiation not only from the emitting object, but also from the surroundings reflected from the object's surface. Figure 9 illustrates the reflection and emission of radiation from a surface.

Thermal
Imaging
System

Reflected

Emitted
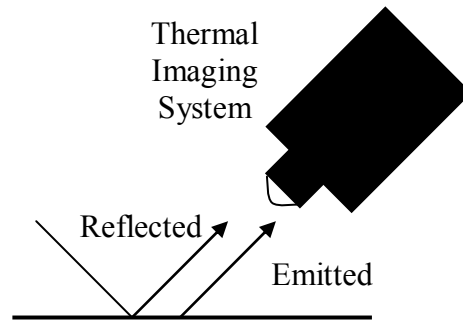
Figure 9. Surface Reflection and Emission[17]

The atmosphere both absorbs and scatters radiation as it travels from the object to the camera, known as the atmospheric transmission.[17] The atmospheric transmission for a 10-meter path length can be seen in Figure 10. It reveals an atmospheric transmission of approximately 0.95 for the wavelength region between nine and twelve micrometers. This is the common spectral range for most infrared cameras.
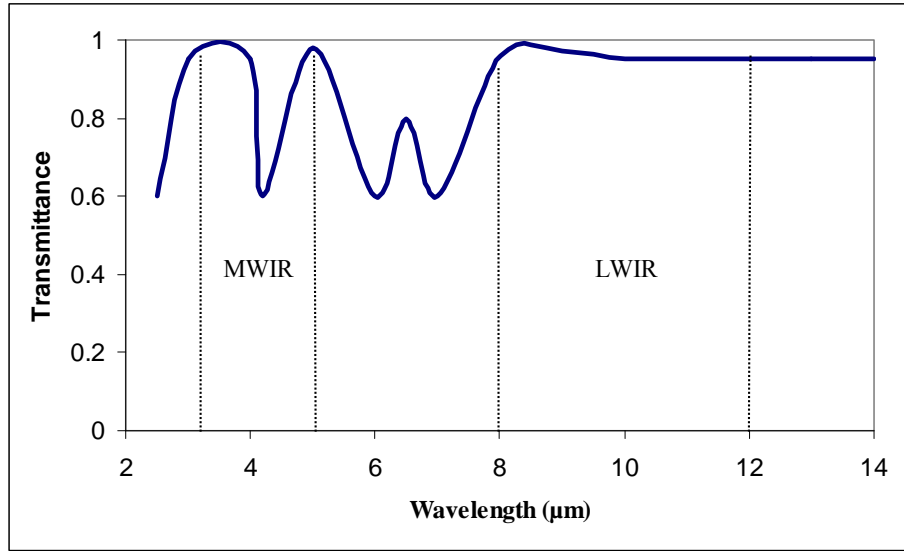
Figure 10. Atmospheric Transmission for a 10 Meter Path Length[17]

Figure 11 describes the general thermographic measurement situation and all the radiation components collected by the infrared camera.
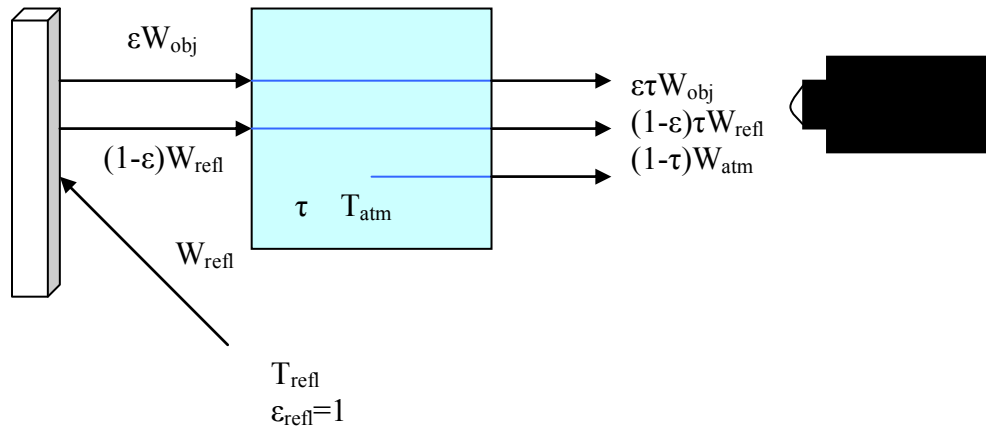
Figure 11. Schematic of Thermographic Measurement[18]

Equation (22) shows the total received radiation power received by the camera, accounting for the emitted radiation from the object, reflected radiation from the object, and emitted atmospheric radiation.

$$W_{tot} = \varepsilon\tau W_{obj} + (1-\varepsilon)\tau W_{refl} + (1-\tau)W_{atm} \qquad (22)$$

W_{tot} is the total received radiation power, ε is the emittance of the object and τ is the

transmittance of the atmosphere. $\varepsilon\tau W_{obj}$ is the emission from the object, $(1-\varepsilon)\tau W_{refl}$ is the

reflected emission from ambient sources and $(1-\tau)W_{atm}$ is the emission from the

atmosphere. The camera output signal is proportional to power input.[18] Within the

camera, the radiation power is converted to a voltage according to Equation (23).

$$U_{source} = CW_{source} \qquad (23)$$

U is the voltage, W is the radiation power, and C is the proportionality constant.

Equation (24) is the voltage equation, which converts voltage to an object temperature.

$$U_{obj} = \frac{1}{\varepsilon\tau}U_{tot} - \frac{1-\varepsilon}{\varepsilon}U_{refl} - \frac{1-\tau}{\varepsilon\tau}U_{atm} \qquad (24)$$

U_{obj} is the calculated camera output voltage for a blackbody of temperature T_{obj}. This

voltage directly converts into object temperature.[18] U_{tot} is the measured camera output

voltage for the actual case. U_{refl} is the theoretical camera output voltage for a blackbody

of temperature T_{refl} according to calibration. U_{atm} is the theoretical camera output voltage

for a blackbody of temperature T_{atm} according to calibration. The camera operator

supplies the values of the object emittance, relative humidity, atmospheric temperature,

reflected temperature and the distance from the object to the camera. The camera

software internally calculates the transmission of the atmosphere from the distance,

atmospheric temperature and relative humidity values.

Magnet Temperature Effects

Hall thrusters require a magnetic field to operate, and magnetic strength is a function of temperature. As the magnet temperature increases, the magnetization of the material decreases until it reaches the Curie temperature. Once the magnet reaches the Curie temperature, its magnetization becomes zero.[6] Figure 12 displays the magnetization relationship with temperature for iron loaded with silicate.[19]
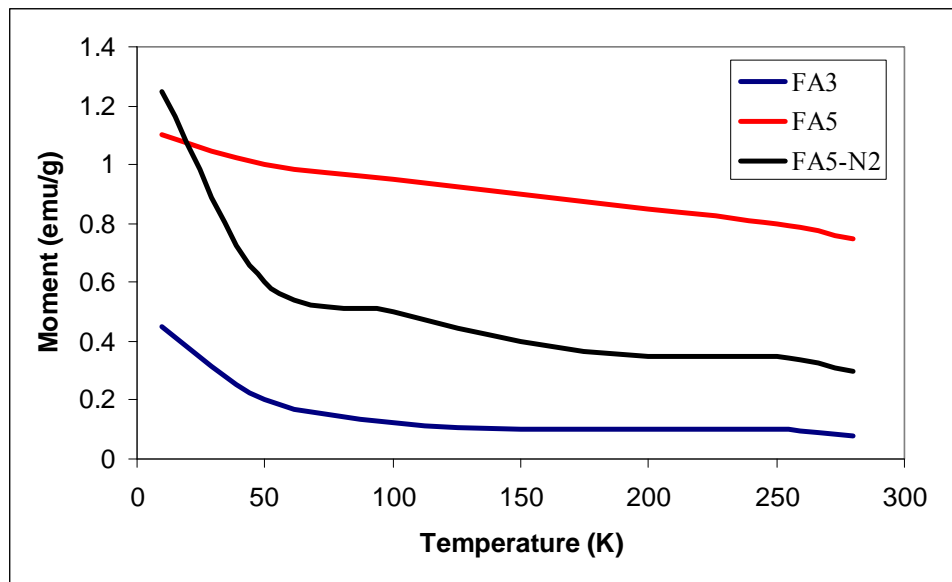
Figure 12. Temperature Effects of Magnetization for Iron[19]

For iron based magnets, temperature increases cause a decrease in magnetic strength. These effects depend on the type of magnet. Table 3 shows the Curie temperatures for several different materials.

Table 3: Curie Temperatures for Various Materials[6]

Material	Curie Temperature
Iron	770 °C
Nickel	358 °C
Cobalt	1130 °C
Gadolinium	20 °C
Terfenol	380-430 °C
Alnico	850 °C
Hard Ferrites	400-700 °C
Barium Ferrite	450 °C

Hall Effect thrusters generally use iron magnets with a Curie temperature of 770 °C. Decreasing the magnetic strength decreases the thruster's efficiency, and magnet failure causes thruster failure.

Anode Temperature Effects

Erosion of the anode channel wall, to the point where the magnetic coils become exposed to the plasma flow is the main source of failure in Hall thrusters.[20] As the high-energy ions collide with the channel wall, the channel wall ejects atoms. This effect is known as sputtering. As more ions and electrons collide with the anode wall, the wall temperature and sputtering increase. As sputtering increases, so does the erosion rate. Figure 13 demonstrates the inner and outer wall thickness as a function of time at the exit plane of a SPT-100 type Hall thruster.
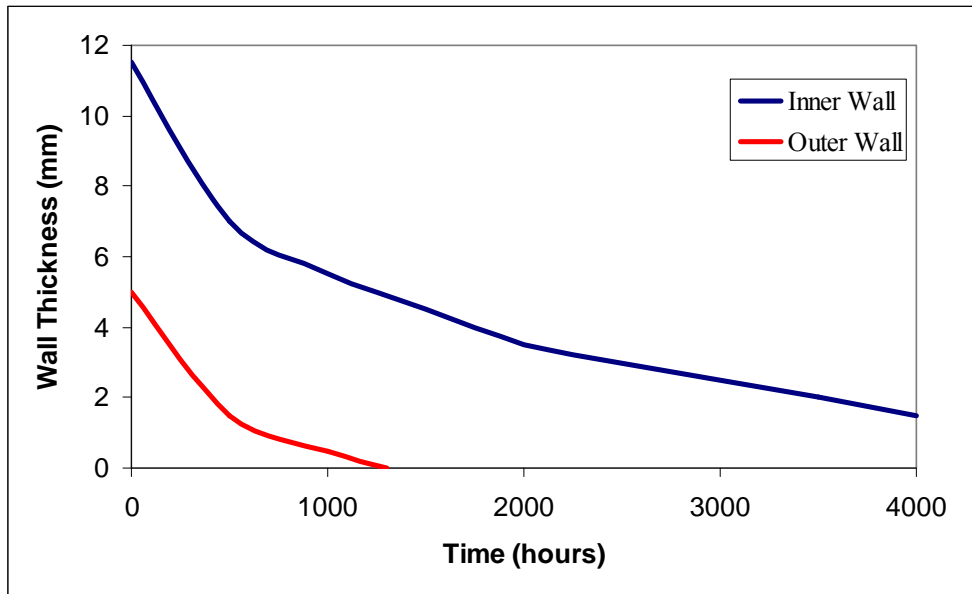
Figure 13. Wall Thickness versus Time at the Exit Plane[20]

The erosion of the anode also leads to a decrease in electric potential. The following

figure shows the potential drop over time as the anode erodes away.
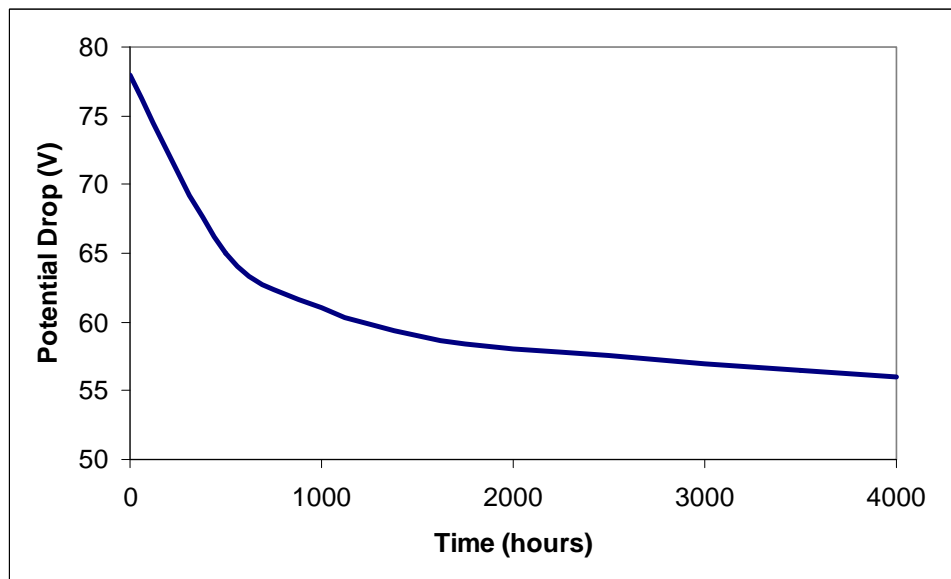
Figure 14. Potential Drop versus Time[20]

A decrease in electric potential decreases the total thrust. Figure 15 illustrates the thrust

over time for a SPT-100 type Hall thruster.
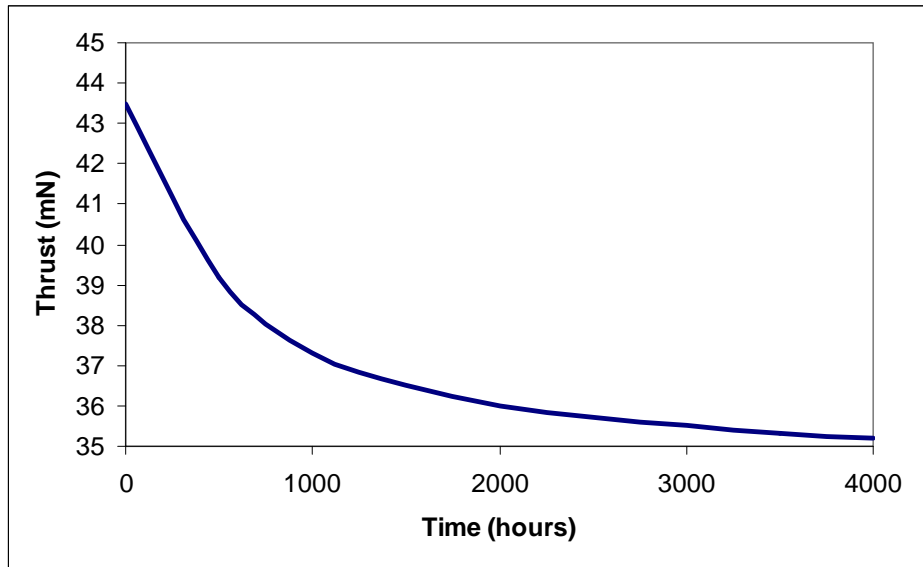
Figure 15. Thrust versus Time[20]

Erosion of the anode causes thrust to decrease.

Cathode Temperature Effects

A hollow cathode consists of a heater, keeper, cathode tube and a low work

function insert. A schematic of a hollow cathode can be seen in Figure 16.
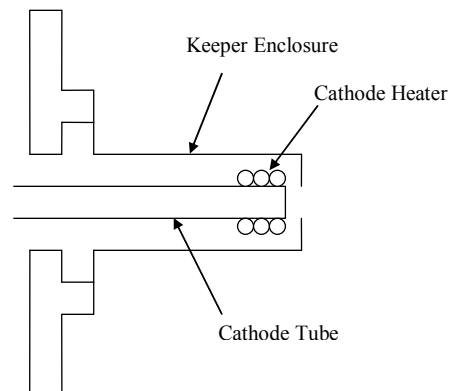
Figure 16. Cut Out of a Hollow Cathode Schematic[21]

Current runs through the cathode heater, causing the insert to increase in temperature and

release electrons from its surface. The emission relates to the exponential of the inverse

of the temperature.[22] These electrons collide with the neutral propellant atoms to create plasma. The keeper then draws the electrons out of the cathode. Reducing the temperature gradient within the cathode insert increases the life of the hollow cathode.[22]

Thermal Imaging Research

Thermal imaging is a growing technology in both military and civilian applications. One application of thermal imaging is night vision reconnaissance. These devices penetrate smoke, fog, haze, snow, and other limitations and can recognize camouflage.[23] The technology is widely used in early warning, searching and tracking, strategic and imaging missile guidance, booster stage monitoring and tracking, air-based and outer atmospheric reentry interception, and mechanical and satellite remote sensing.[23] In the civilian industry, thermal imaging applies primarily to production monitoring and non-destructive materials inspection.[23] Thermal imagers demonstrated the capability to do stress analysis in the testing of full-scale wind turbine blades.[24] In 1989, thermal imaging analyzed the complex flow dynamics and combustion process involved in the mixing of hot fuel rich jets and air.[25] Infrared imaging has also been used to study the boundary layer transition surface temperatures of the Space Shuttle during reentry.[26] Thermal imaging can also help in the diagnosis of illness.[23] An example of this is using breast thermograms for cancer diagnosis.[7]

Previous Research

Use of infrared thermal imaging also found its way into Hall thruster research. A recent study monitored wall temperatures to obtain new insights into plasma surface interactions inside the thruster.[27] For a given thruster geometry and material, this study

23

found a relationship between the mean wall temperature and electrical input power.[27] Current research by the Air Force Research Laboratory at Edwards Air Force Base used thermographic imaging to analyze a 200 and 600 Watt Hall thruster. Imagery of thruster start up, steady state and shut down was used to approximate heating behavior.[28] Figure 17 shows a temperature profile for several parts of the 200 Watt Hall thruster. This study revealed the highest temperature regions of the 200 Watt thruster to be the anode nose cone and the cathode tip. The anode nose cone's steady state temperature was 400 °C, and the steady state temperature of the cathode tip was 375 °C. The study also showed the thruster components needed 250 minutes to cool down to original temperatures.
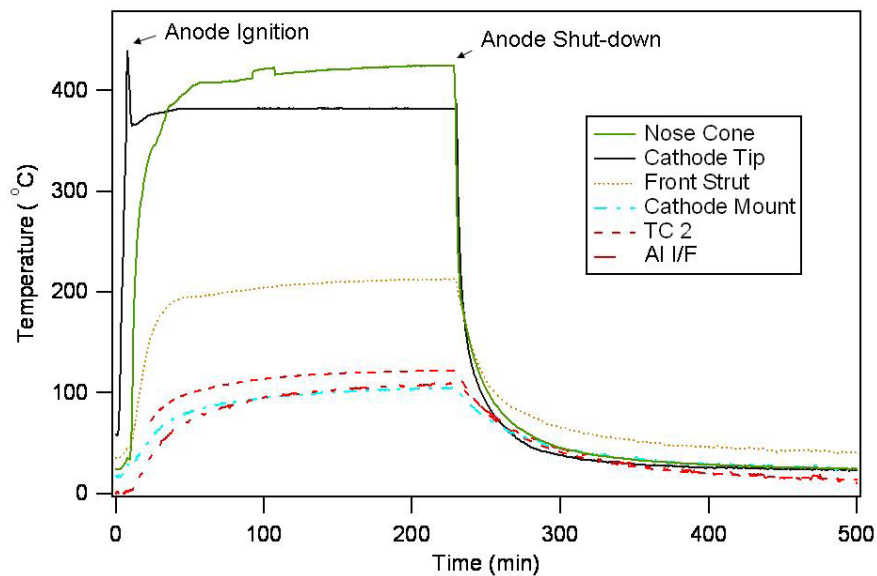
Figure 17. 200 Watt Thruster Temperature versus Time for a 3.5 Hour Nominal Burn[28]

Previous research at the Air Force Institute of Technology also studied a Hall thruster using thermal imaging.[29] Figure 18 shows an image taken of the thruster at an angle of 45 degrees to the camera. The image exhibits saturation in the center of the Hall thruster at the anode nose cone.

Figure 18. Image of Hall Thruster at 45 Degree Angle to Camera[29]

The camera used in this experiment peaked at 773 K. This study concluded that future thermal research of a Hall Effect thruster should use a camera with a higher maximum temperature, and that calculating the view factors between thruster components would increase the accuracy of the temperature data. Current work, accomplished in this research, includes a camera with a higher maximum temperature and a view factor analysis on a section of the cathode to determine increased accuracy.

Infrared Camera

The camera chosen for this research is the FLIR, ThermaCAM SC640. The following figure shows a picture of the ThermaCAM SC640 infrared camera. This camera was chosen for this experiment because of the high measurement temperature range. Previous research revealed saturation of the camera occurring around 500 °C. Table 4 shows the camera's specifications.

Figure 19. ThermaCAM SC640 Picture[30]

Table 4: ThermaCAM SC640 Technical Data[30]

Detector Type	Focal Plane Array (FPA)
Spectral Range	7.5 to 13 µm
Resolution	640 X 480 pixels
Temperature Range	-40 °C to 1500 °C Optional up to 2000 °C
Accuracy	±2 °C, ±2% of reading
Interfaces	Firewire, USB, IrDA, SD-card

III. Methodology

Chapter Overview

     The purpose of this chapter is to describe the laboratory setup and the data taken during the experiment. First is a description of the Hall thruster used in the experiment. This is followed by a description of the emissivity tests and data collected. The last part of this chapter describes the Hall thruster vacuum test and data collected.

Hall Thruster

     The thruster used in this experiment was a 200 Watt Hall Effect thruster manufactured by Busek Co. Inc. The front, side and rear views of the thruster can be seen in Figure 20.
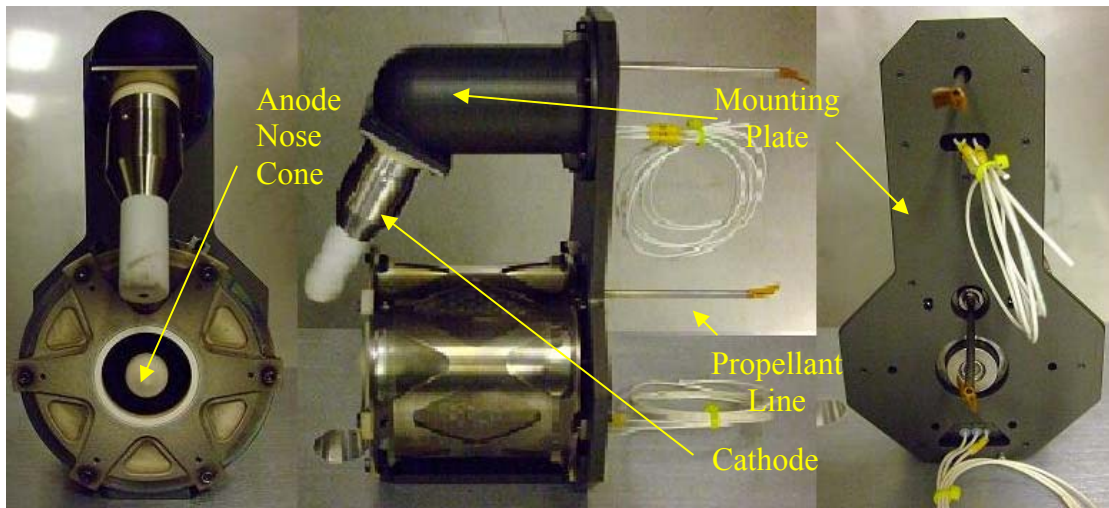
Figure 20. Front, Side and Rear View of Thruster

The front view shows the location of the anode nose cone and the thruster chamber. The location of the cathode is above the chamber. The mounting plate connects the cathode to the thruster chamber, and provides an interface for the propellant lines and electrical connections. According to Busek, the thruster has the following specifications.[31]

27

Table 5: Busek 200 W Thruster Specifications[31]

Discharge Input Power	200 W
Discharge Voltage	250 V
Discharge Current	800 mA
Propellant Mass Flow Rate	0.94 mg/sec
Thrust	12.8 mN
Specific Impulse	1390 sec
Propulsive Efficiency	43.5%

The front view of the thruster in Figure 20 shows some discoloration on the exit

plane and cathode portion of the thruster. This is due to the manufacture's testing and

experimental setup testing. The manufacture's testing consisted of an unknown number

of hours, while the experimental setup consisted of approximately 5 hours. Since

emissivity depends on the nature of the surface coating, the discoloration can affect the

values for the different parts of the thruster.[14]

Vacuum Chamber

The vacuum chamber used in this experiment was located in the Space Propulsion

Analysis and System Simulator (SPASS) Laboratory at the Air Force Institute of

Technology (AFIT) on Wright-Patterson Air Force Base. The SPASS Laboratory

vacuum chamber can be seen in Figure 21. It is 2.0 m (6.6 feet) in diameter and 3.1 m

(10 feet) long, and has a two stage pumping scheme. A Leybold-Trivac rotary vacuum

pump brings the pressure down from atmospheric to 80 mtorr.

Figure 21. SPASS Laboratory Vacuum Chamber

Four 20 inch CVI Torrmaster cryogenic pumps decrease and maintain the pressure to as low as 3×10^{-8} torr. The measured pumping speed of the system is approximately 16,000 liters per second for xenon.

The vacuum chamber has two gauges that monitor the pressure. From atmospheric to 80 mtorr, a Kurt J. Lesker mini-convectron gauge monitors the pressure. Labview records and logs this pressure data. An ExTorr residual gas analyzer (RGA) monitors the high vacuum pressure. The RGA software monitors the partial pressures of each atomic mass and the total pressure.

Chamber Window

The experiment requires a window with a high transmissivity because the infrared camera is outside the vacuum chamber. The high transmissivity allows greater amounts of radiation to reach the infrared camera. The material chosen for the window was zinc selenide (ZnSe). ZnSe has a high transmission percentage in the range of the infrared camera, which is 7.5 to 13 μm. Figure 22 illustrates the transmission percentage for a 10 mm thick the window.
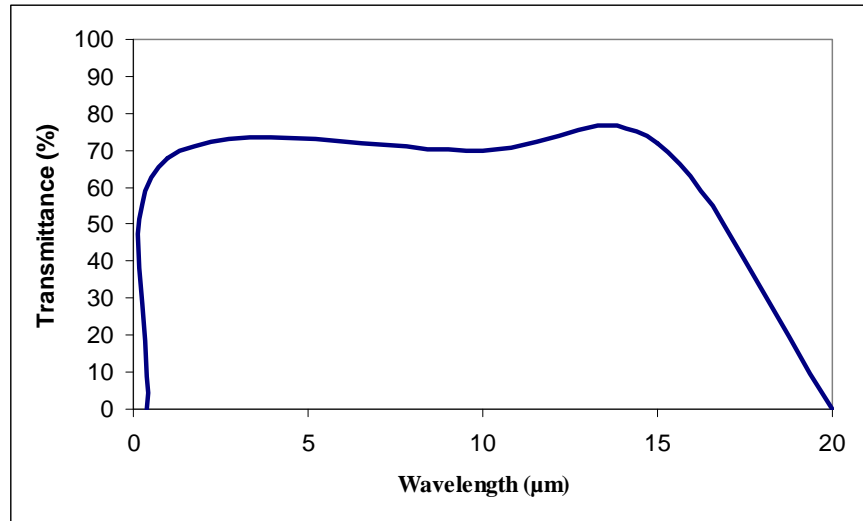
Figure 22. Transmission Percentage for a 10 mm Thick ZnSe Window[32]

The ZnSe window chosen for the experiment was 12.7 cm (5.0 inches) in

diameter and 10 mm (0.394 inches) thick. A specially manufactured viewport, with a

viewing window of 11.4 cm (4.5 inches), mounted the ZnSe window to the vacuum

chamber. Figure 23 shows the viewport and the ZnSe window attached to the vacuum

chamber.
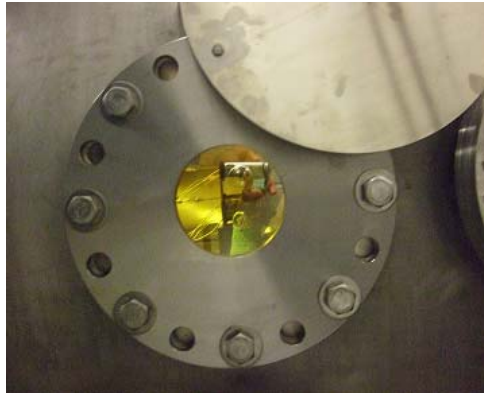
Figure 23. ZnSe Window and Viewport

Detailed mechanical drawings of the viewport setup can be seen in Appendix D.

The infrared camera and the ThermaCAM Researcher software verified the transmission percentage of the ZnSe window. The test included five data points at a range of temperatures. At each temperature, two images were taken with the infrared camera, one with the ZnSe window and one without. Figure 24 shows an image of the boron nitride sample without the ZnSe window and Figure 25 shows an image of the boron nitride sample with the ZnSe window.
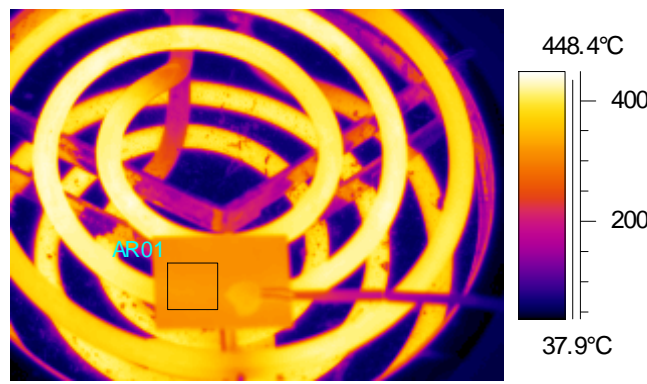
Figure 24. Transmission Test without the ZnSe Window
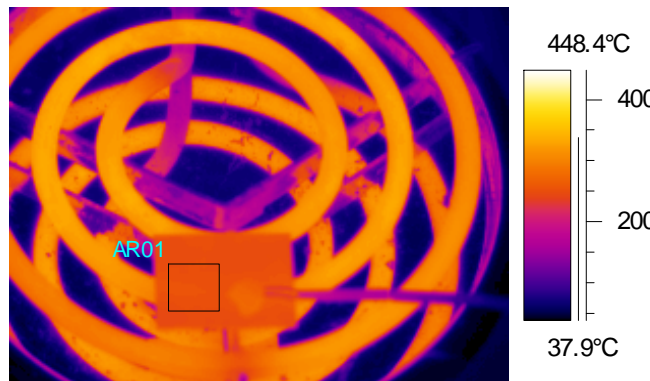
Figure 25. Transmission Test with the ZnSe Window

The software then adjusts the external optics transmission so the temperatures of the two images match. Figure 26 shows the transmission percentage versus temperature for the ZnSe window. The error bars include the thermocouple and camera error.
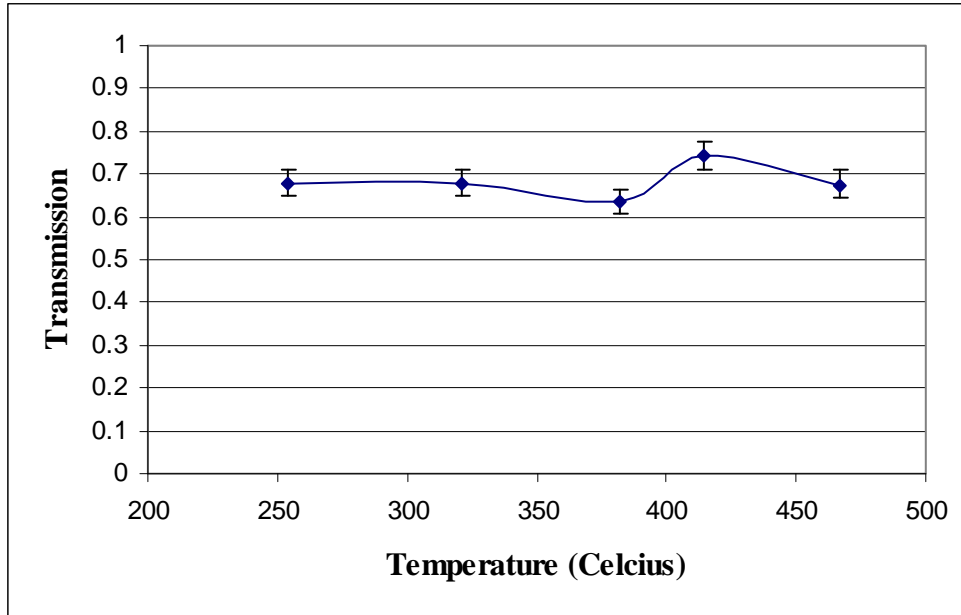
Figure 26. Transmission versus Temperature for the ZnSe Window

The average transmissivity of the temperature range is 0.682 with a standard deviation of 0.038. This value agrees with Figure 22, showing a 70% transmission for the ZnSe window.

Experimental Setup

The thruster mounts inside the vacuum chamber, centered in the ZnSe window. This provides an optimal view for the infrared camera located outside the chamber. Figure 27 shows the experimental setup viewed from the vacuum chamber door. The distance between the ZnSe window and the centerline of the thruster was 1.17 m (46 in). The infrared camera, located outside the vacuum chamber, was 0.15 m (6 in) away from the ZnSe window. At this distance, the thruster filled a 150 x 240 pixel area.

The propellant used in the experiment, for both the anode and the cathode, was grade five xenon. Flow was controlled by two MKS flow meters and an MKS type 247

4-channel readout. The anode flow meter was calibrated for 0-50 standard cubic

centimeters (sccm) of xenon, and the cathode flow meter was calibrated for 0-10 sccm of

xenon.
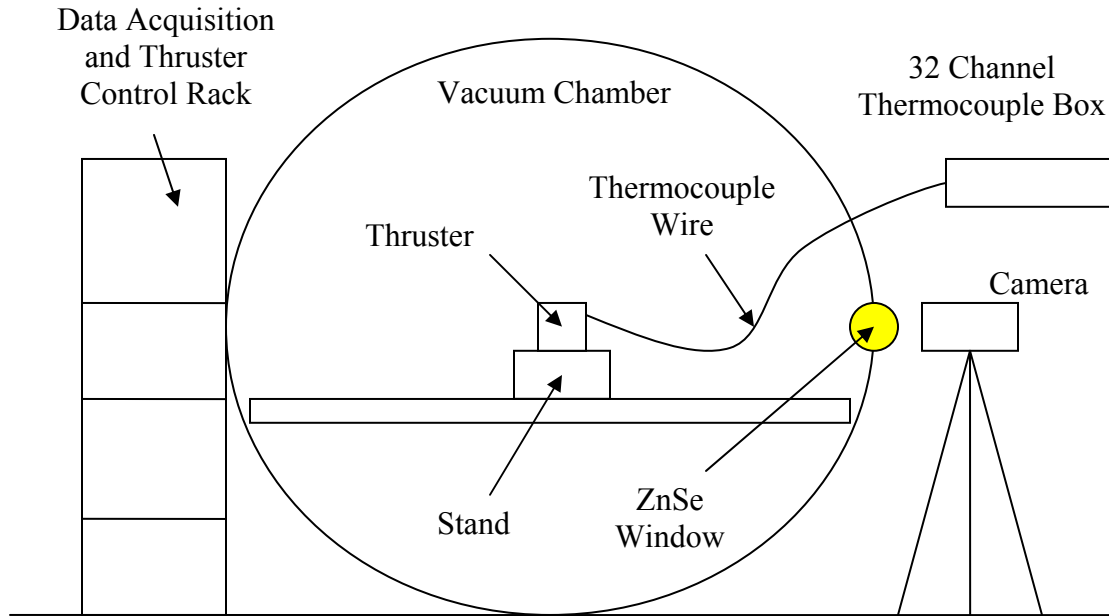
Figure 27. Experimental Setup

Thermocouples anchor the camera data and provide confidence in the temperature

data. They run through feedthroughs on the chamber wall and connect to a National

Instruments TC-2095 32-Channel Thermocouple Connector. A National Instruments

SH96-96 Shielded Cable connected the 32-channel connector to a National Instruments

SCXI-1102 32-Channel Thermocouple Amplifier. This plugged into a National

Instruments SCXI-1001 12-Slot Chassis, which connects to the thermocouple computer

by USB. The software used to record and save the thermocouple data was LabVIEW®.

Thermocouples

Six type K thermocouples validate the camera temperature measurements. The uncertainty values of the thermocouples are the greater of ±0.75% or ±2.2°C. The thruster had five thermocouples epoxied to the surface and one was attached to the chamber wall using Kapton tape. Attached to the boron nitride material on the lower, front part of the thruster was Thermocouple 1. This can be seen in Figure 28.

Figure 28. Thermocouple 1 Location

Figure 29 shows the location of Thermocouple 2, located on the alumina plasma sprayed portion of the cathode.

Figure 29. Thermocouple 2 Location

Thermocouple 3 is attached to the stainless steel portion of the cathode, and Thermocouple 4 is attached to the stainless steel side of the thruster. Both are shown in the next figure.
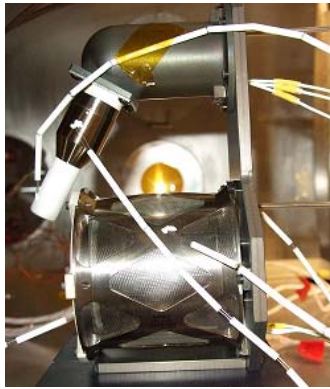
Figure 30. Thermocouple 3 and 4 Location

Figure 31 shows the location of Thermocouple 5, which is on the anodized aluminum portion of the backside of the thruster.
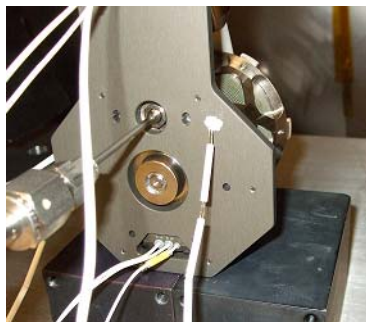
Figure 31. Thermocouple 5 Location

The last thermocouple is on the vacuum chamber wall underneath the ZnSe window, and is shown in the following figure.

Figure 32. Thermocouple 6 Location

Thermocouple 6 is the only one attached with Kapton tape.

Emissivity Tests

The most important factor in radiation is emissivity. It measures the emitted radiation from an object, compared to that from a perfect blackbody of the same temperature.[18] The Hall thruster consists of four main materials: boron nitride, stainless steel, anodized aluminum, and alumina plasma sprayed stainless steel. Figure 33 illustrates the locations of these materials on the thruster.
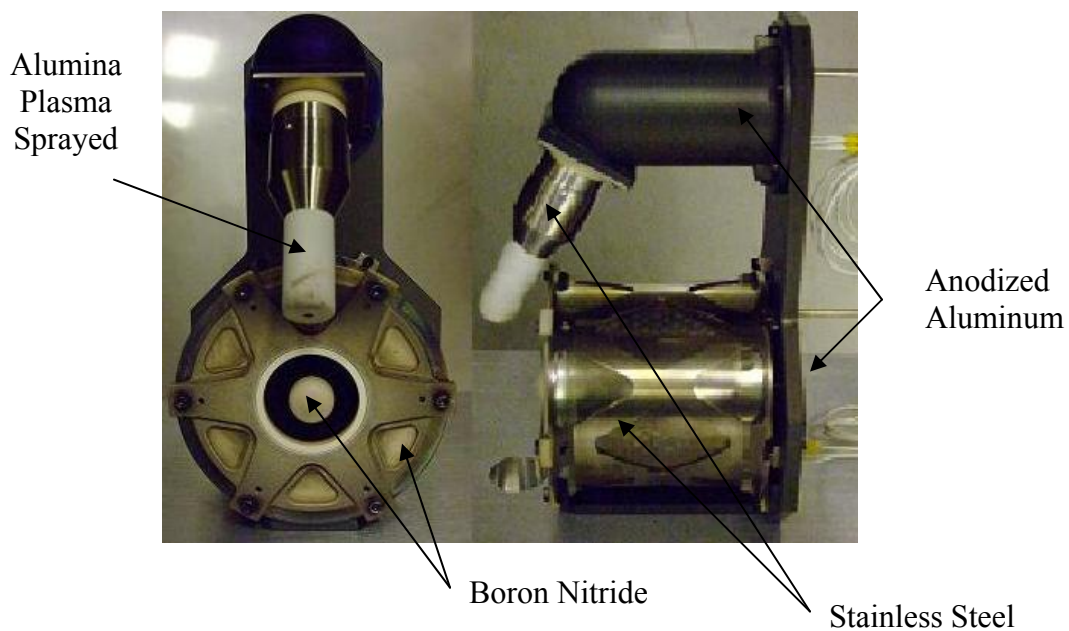
Figure 33. Hall Thruster Materials and Location

Busek Co. Inc. supplied samples of each material, so that emissivity values could be determined experimentally.

The emissivity values were determined experimentally using the ThermaCAM SC640, type K thermocouples, and the ThermaCAM Researcher software. The thermocouples were attached to each sample using a high temperature ceramic epoxy. A hot plate then heated each sample to various temperatures, and the infrared

camera captured the thermal image. The camera requires several inputs before capturing

an image. The first is the reflected apparent temperature. This parameter compensates

for the background reflected radiation.[18] Appendix A shows the procedures for

determining the reflected apparent temperature.[18] The camera also requires the distance

from the object to the camera, the relative humidity and the atmospheric temperature.

Appendix B shows the camera emissivity test procedures.[18] Table 6 displays the camera

inputs for each emissivity test.

Table 6: Camera Inputs for Emissivity Tests

Sample	Stainless Steel	Boron Nitride	Alumina Plasma Sprayed	Anodized Aluminum
Reflected Apparent Temperature (°C)	29.6	27.6	23.2	23.0
Atmospheric Temperature (°C)	25.5	23.8	22.7	21.6
Distance (m)	0.8	0.8	0.9	0.8
Humidity (%)	30	30	30	30
Emissivity	1	1	1	1

Along with each thermal image, the thermocouple data was recorded. Post-

processing of the thermal image required the ThermaCAM Researcher software.

ThermaCAM Researcher has several tools to analyze image temperatures. The spot

meter tool analyzes one spot on an image. The line tool analyzes minimum, maximum

and average temperatures along a straight line within the image. The area tool measures

the maximum, minimum, and average temperatures in a box, circle, or polygon. The

software adjusts the emissivity value, so that the sample temperature matched the thermocouple temperature. Appendix C shows the emissivity calculation procedures using the ThermaCAM Researcher software.[33]

Each emissivity test consisted of five data points, taken at various temperatures and analyzed with the software. The uncertainties include the thermocouple error and the camera error of $\pm 2\%$ or ± 2 °C. Figure 34 is an example of the stainless steel thermal image, which used the line area tool to account for the cylindrical geometry.
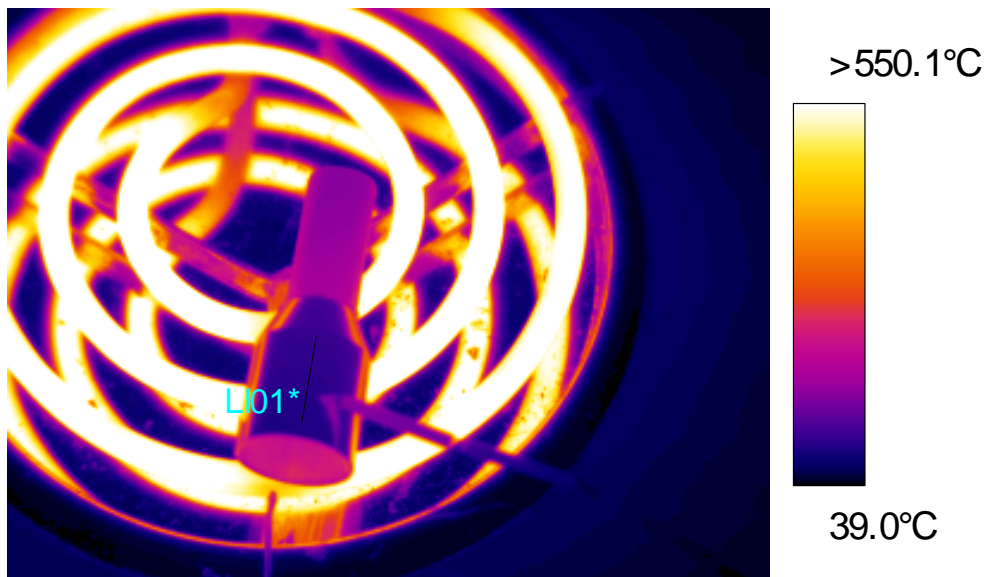
Figure 34. Stainless Steel Emissivity Test Image

Figure 35 shows the results of the emissivity test for the stainless steel sample. The temperature range for the stainless steel test was 50 °C to 250 °C. The emissivity of the stainless steel increases with temperature.

The boron nitride sample used the box area tool to calculate the emissivity. Figure 36 shows an example of the boron nitride sample test. The emissivity and uncertainties for the boron nitride sample can be seen in Figure 37 with a temperature

range between 275 °C and 530 °C. The emissivity remains relatively constant across this
temperature range.
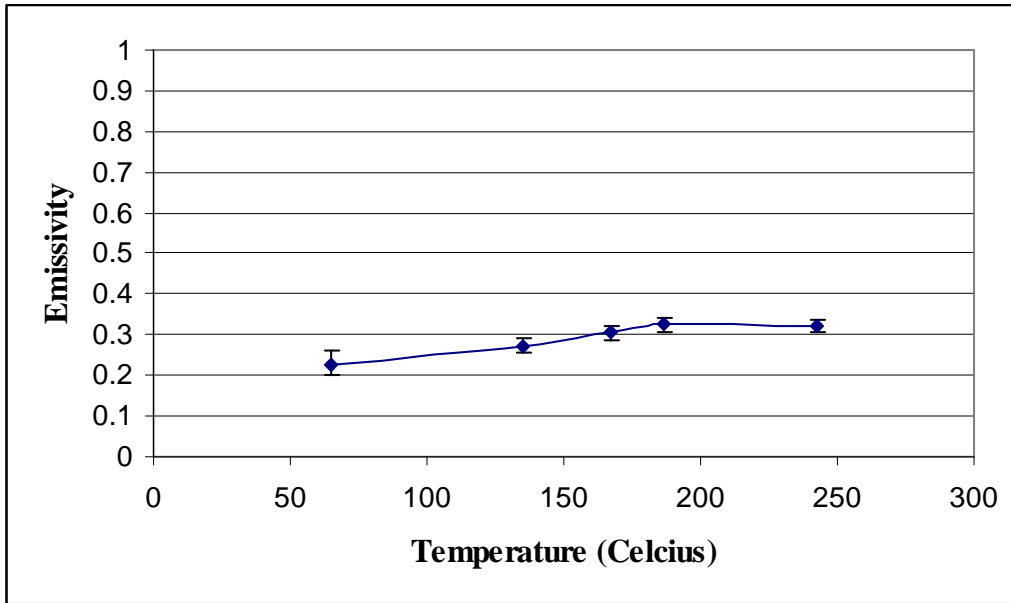
Figure 35. Stainless Steel Emissivity versus Temperature
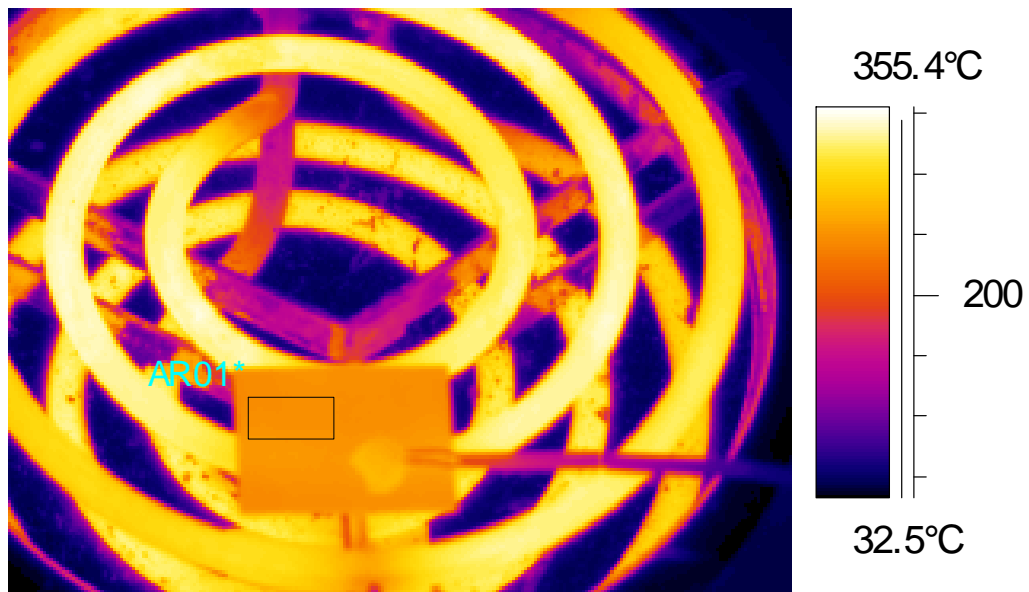
Figure 36. Boron Nitride Thermal Image
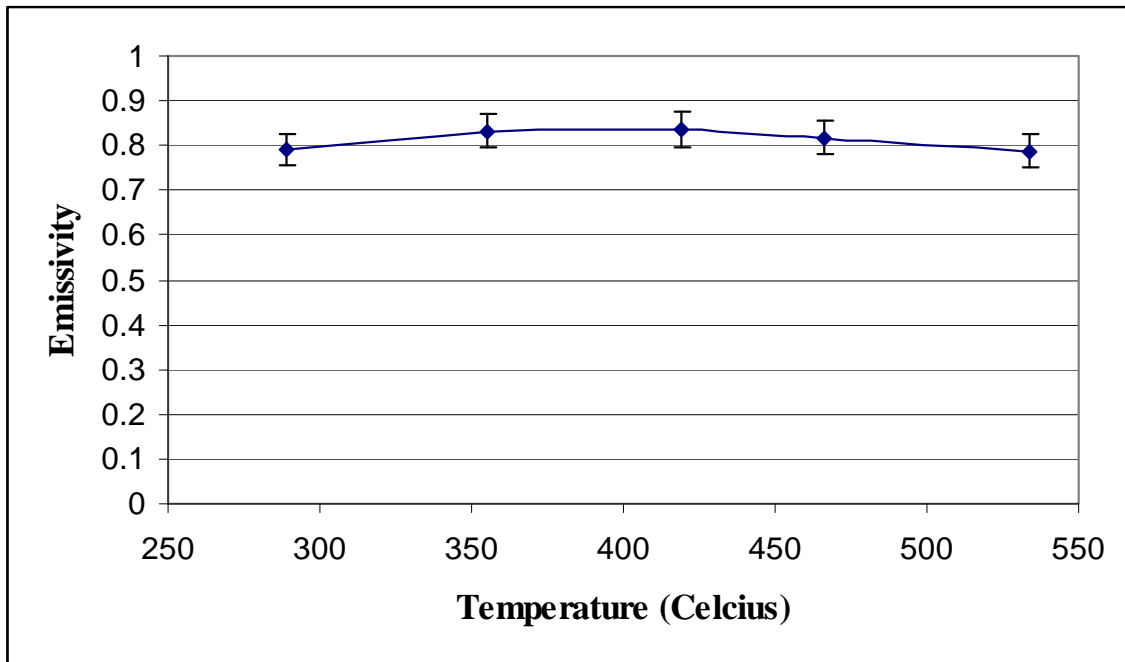
Figure 37. Boron Nitride Emissivity versus Temperature
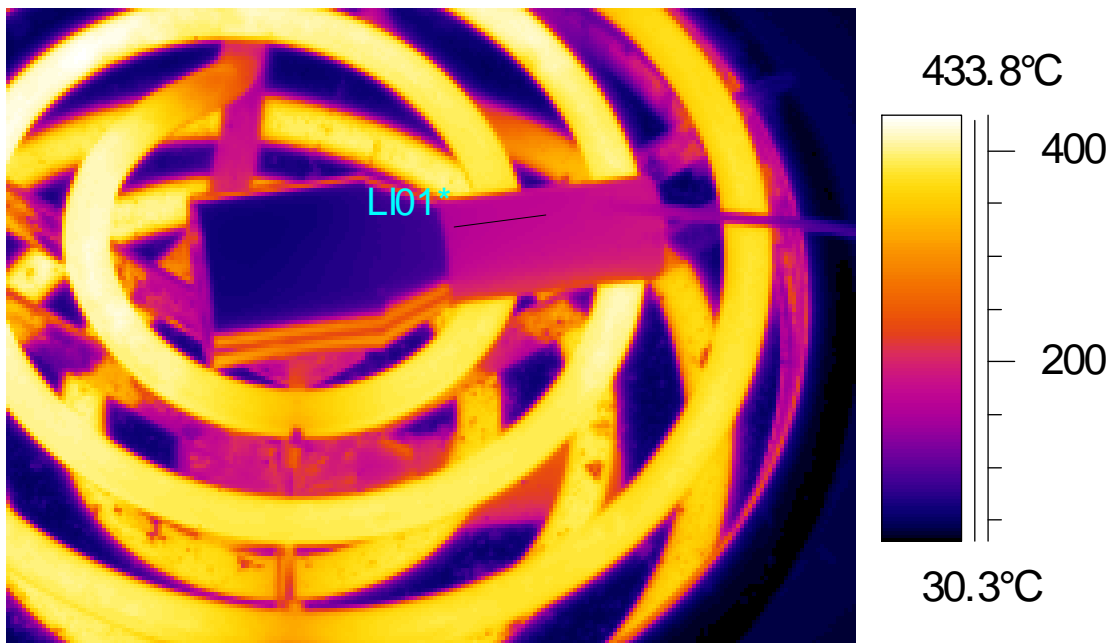
Figure 38. Alumina Plasma Sprayed Stainless Steel Thermal Image

The alumina plasma sprayed stainless steel tests used the line area tool to calculate the average temperature of the sample. The line area tool accounts for the cylindrical geometry of the sample.   Figure 38 displays a thermal image from one of the emissivity tests. The emissivity versus temperature plot for the alumina sample can be seen in Figure 39. The temperature ranged from 150 °C to 325 °C for this test, and the emissivity increased with temperature.
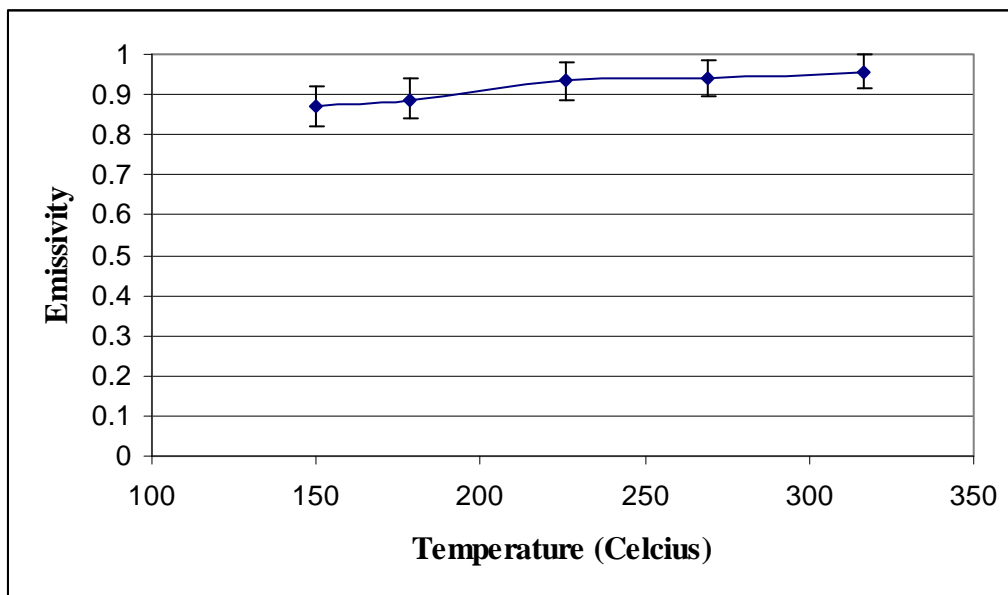
Figure 39. Alumina Emissivity versus Temperature

The final emissivity test was the anodized aluminum sample. For this sample, the box tool analyzed the emissivities. An example of one of the thermal images can be seen in Figure 40. Figure 41 displays the emissivity versus temperature plot for the anodized aluminum sample. The temperature ranged from 40 °C and 150 °C. The emissivity increased with temperature until approximately 90 °C, and remained constant for the rest of the temperature range.

41
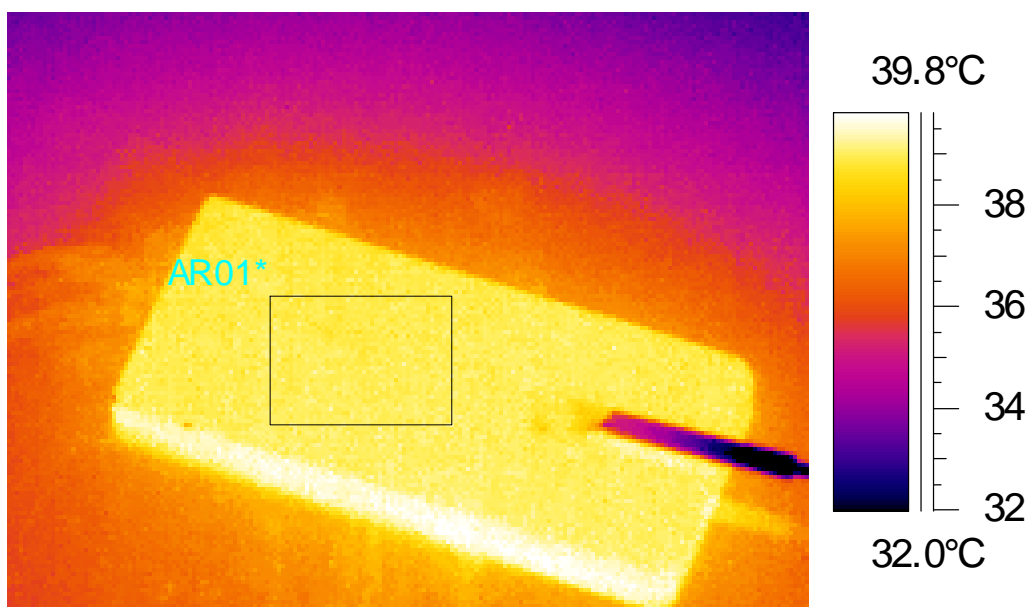
Figure 40. Anodized Aluminum Thermal Image
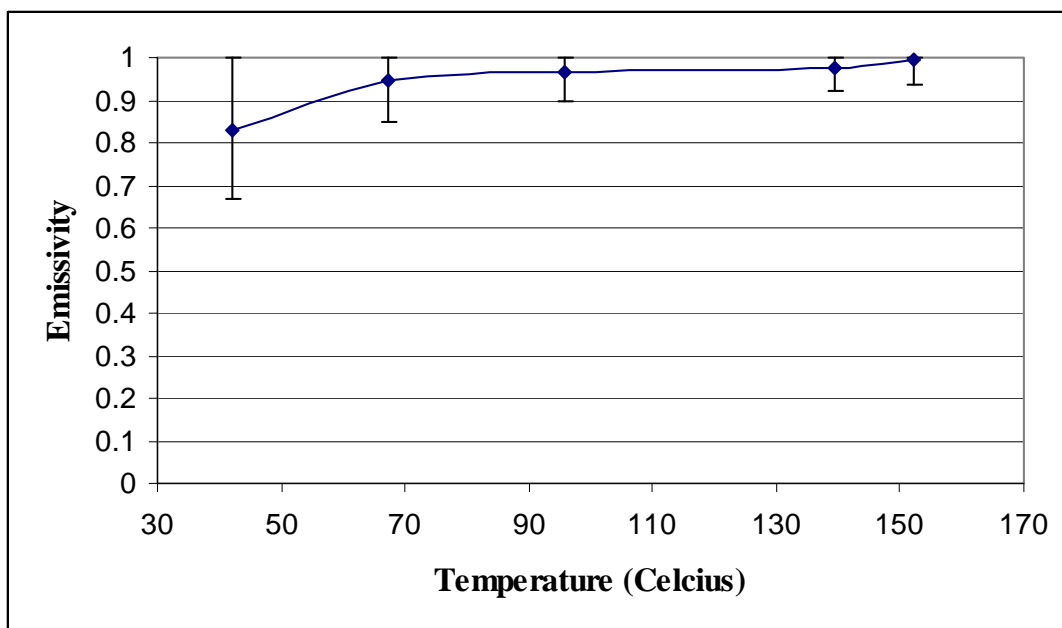
Figure 41. Emissivity versus Temperature for Anodized Aluminum Sample

Table 7 shows the average emissivities and standard deviations for each sample over their temperature range.

Table 7: Test Sample Average Emissivities and Standard Deviations

Sample	Average Emissivity	Standard Deviation
Stainless Steel	0.290	0.041
Boron Nitride	0.811	0.023
Alumina Plasma Sprayed	0.917	0.027
Anodized Aluminum	0.943	0.065

Data Collection

For this experiment, data was collected from four different tests. Each test included the thruster operating during start up, steady state and shut down. During the first two tests, the camera viewed the side of the thruster. The last two tests had the thruster rotated 30 degrees towards the camera. Each position required two tests because of the infrared camera's temperature range, which limits the overall temperature measurement. The ThermaCAM SC640 has three range settings: -40 °C to 120 °C, 0 °C to 500 °C, and 300 °C to 2000 °C. Table 8 displays the date and camera setting for each experiment.

Table 8: Camera Settings for Each Test

Date	29 Oct 07	30 Oct 07	3 Nov 07	4 Nov 07
Reflected Apparent Temperature (°C)	32.6	33.8	50.6	50.6
Atmospheric Temperature (°C)	20.6	20.6	37.2	37.2
Distance (m)	0.2	0.2	0.2	0.2
Humidity (%)	30	30	30	30
Emissivity	1	1	1	1
Transmissivity	0.7	0.7	0.7	0.7
Temperature Range (°C)	0-500	300-2000	0-500	300-2000

For each test, the camera recorded images at a rate of one per minute and stored them on an SD Memory Card.

Appendix E illustrates the thruster start up and shut down procedures.[34] The mass flow rate of xenon was the same for each test. The anode flow rate was 8 sccm and the cathode flow rate was 0.8 sccm. The thruster settings for each experiment can be seen in Table 9.

Table 9: Hall Thruster Experiment Settings

Cathode Heater Current	6.5 A
Cathode Keeper Current	0.5 A
Magnet Current	1.25 A
Discharge Voltage	250 V

Thruster start up took 12 minutes. With the heater current at 6.5 A, it took 8 minutes for the cathode heater voltage to reach 6 V. The keeper current was then applied for 2 minutes, before the magnet current and the discharge voltage was applied simultaneously. After running for two more minutes, the cathode could sustain operating without the heater current, so it was turned off. After turning the heater current to 0 A, the thruster ran for 3.5 hours. The thruster and propellant flow was then shut down and cool down took 4 hours. While the thruster was firing, the vacuum chamber pressure was approximately 2.59×10^{-3} Pa $(1.943 \times 10^{-5}$ Torr).

IV. Analysis and Results

Chapter Overview

This chapter contains the results of start up, steady state, and shut down operation of the thruster. It includes temperature profiles, validated using thermocouples, and heating rates for each thruster operating regime. The last section of this chapter includes the results of applying the view factor correction to the alumina plasma sprayed portion of the cathode.

Thermocouple and Camera Data

The ThermaCAM Researcher software validated the thermocouple data. The software plotted temperature profiles for five spots, corresponding to thermocouple locations, and two spots without thermocouples. Figure 42 shows the first four spots, located on the side view of the thruster, chosen with the software. These four locations represent four of the thermocouples. SP01 corresponds to the stainless steel side of the thruster, and its X and Y locations are 314 and 269. SP02 is along the stainless steel portion of the cathode (X: 374, Y: 207). SP03 is on the anodized aluminum section of the rear base plate (X: 266, Y: 264), and SP04 corresponds to the alumina plasma sprayed portion of the cathode (X: 398, Y: 243).
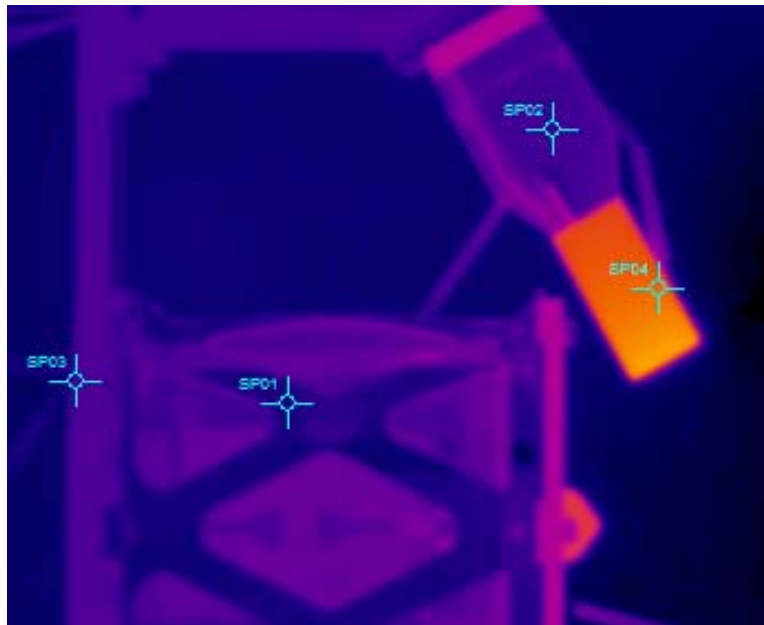
Figure 42. Spot Temperature Locations on Side View

Figure 43 displays the last three spot locations on the rotated view of the thruster.

Figure 43. Spot Temperature Locations on Rotated View

SP01 represents the boron nitride section of the front plate (X: 383, Y: 264) and the

location of a thermocouple. The last two spots could not be validated with

thermocouples, because of the potential interference with the exit plasma. The

installation of thermocouples at this location effects thruster operation. SP02 (X: 403, Y:

241) is on the anode cone, SP03 (X: 403, Y: 230) is on the chamber wall. The material of both these spots is boron nitride.

Figure 44 shows the camera and thermocouple results for the alumina plasma sprayed section of the cathode, using the experimental calculated emissivity of 0.917. The steady state temperature difference between the camera and thermocouple is approximately 165 °C, leading to the result that the thermocouple is malfunctioning. With an experimentally determined emissivity of 0.917, the thermocouple data and camera data should be closer to each other. The alumina surface is rough and the thermocouple did not have good enough contact with the surface to yield accurate results, or it is possible the ceramic adhesive blocked the thermocouple from the surface of the material.
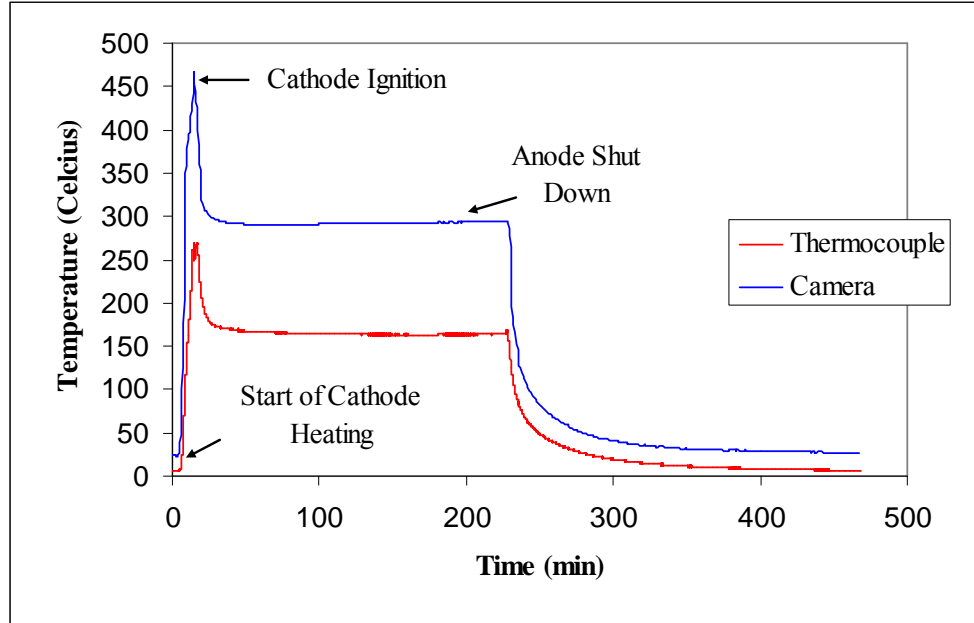
Figure 44. Thermocouple and Camera Data for the Alumina Section of the Cathode

As expected, the temperature increases as current is supplied to the cathode heater and keeper. After anode ignition, electrons flow into the chamber. This creates fewer

collisions along cathode inner wall and the temperature decreases to steady state. The anode temperature decreases to the original temperature once the anode ceases to operate. Figure 45 shows the same results for the stainless steel section of the cathode with an emissivity of 0.29.
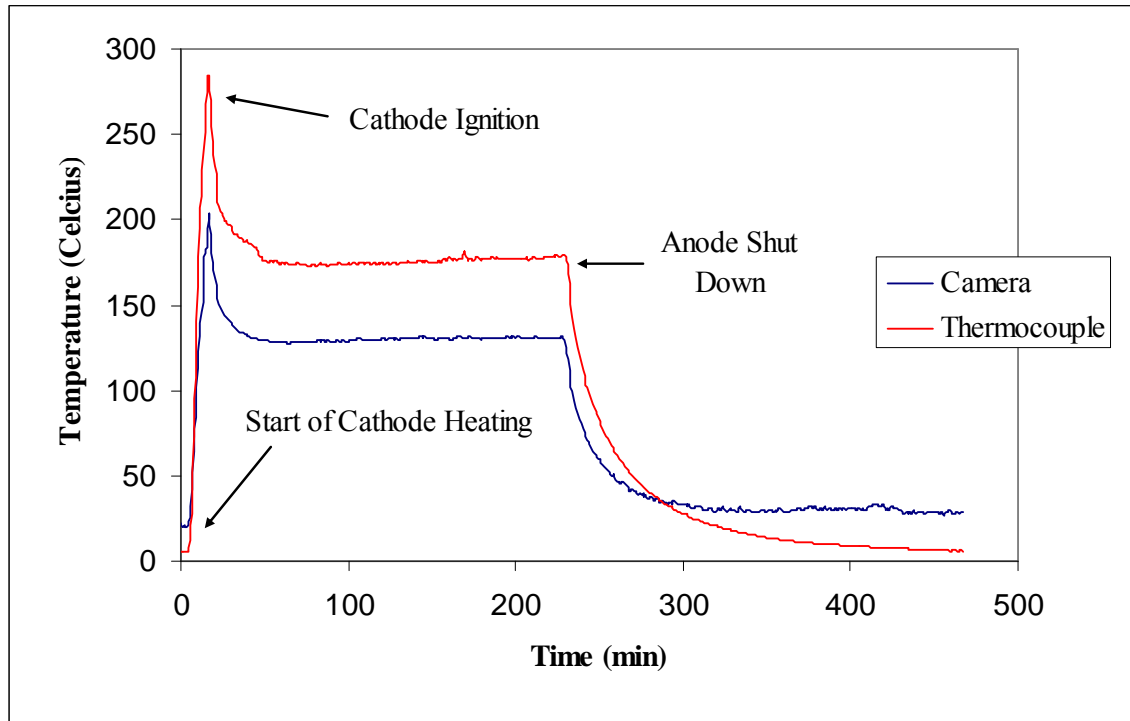
Figure 45. Thermocouple and Camera Data for the Stainless Steel Section of the Cathode

Figure 46 displays the results for the stainless steel side of the Hall thruster with an emissivity of 0.29. The temperature profile for the boron nitride front plate with an emissivity of 0.811 can be seen in Figure 47. The temperature, of both the side of the thruster and the front plate, increases upon the enabling of the magnet and anode current. It reaches steady state at approximately 150 minutes after anode ignition, and decreases in temperature when the anode is shut down.
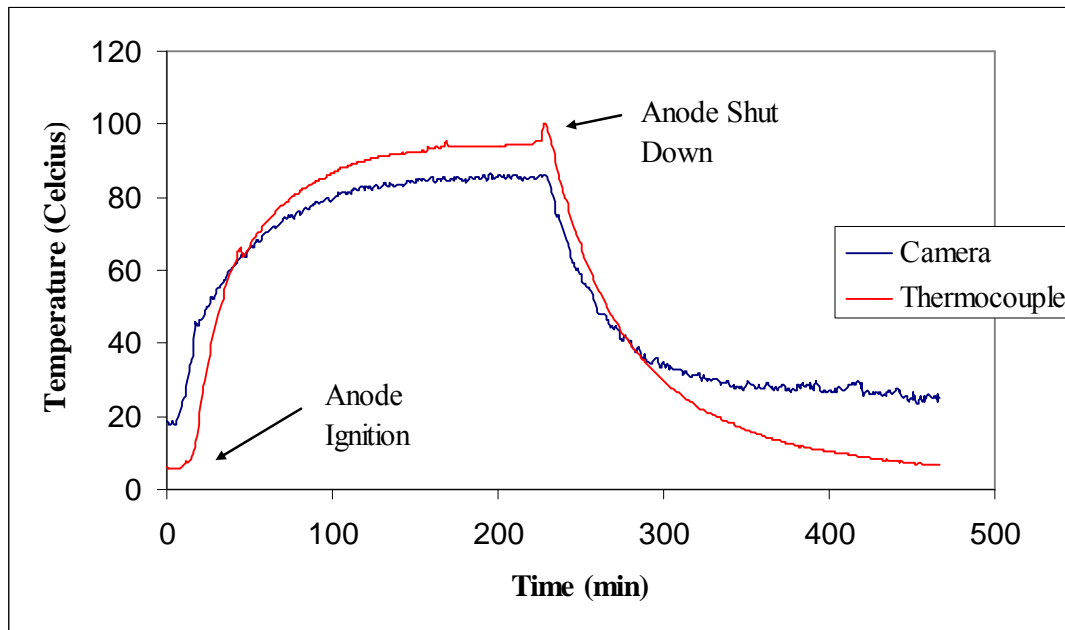
Figure 46. Temperature Profile for the Stainless Steel Side of the Thruster
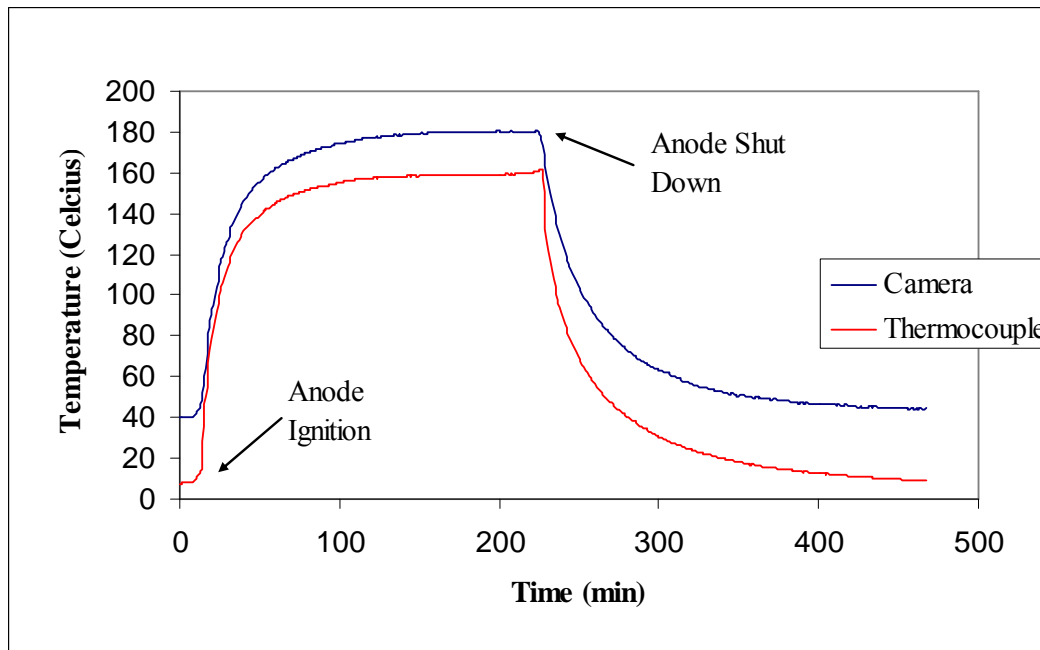
Figure 47. Temperature Profile for the Boron Nitride Front Plate

Figure 48 displays the temperature profile for the anode nose cone and the chamber wall.

Both are boron nitride with an emissivity of 0.811. Both the anode nose cone and

chamber wall heat up after anode ignition. The steady state temperature of the anode

nose cone is 217 °C and the steady state temperature of the chamber wall is 211 °C.

These temperatures relate directly to the erosion rate of the anode due to sputtering.
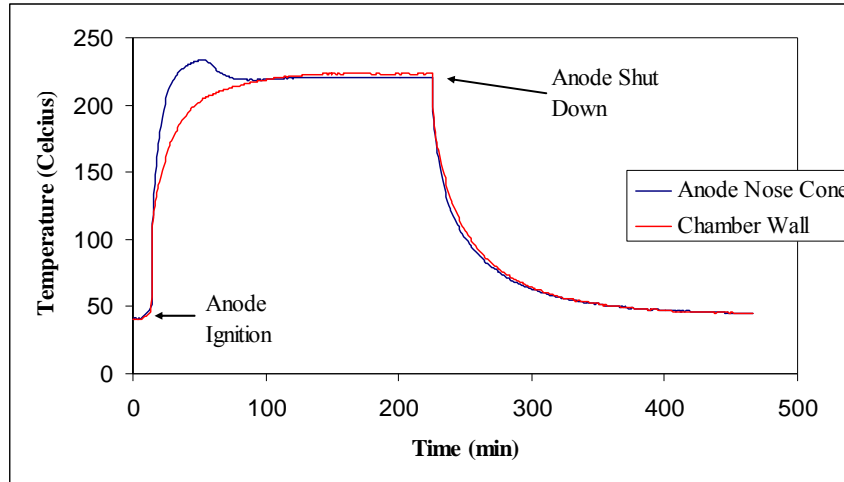
Figure 48. Temperature Profile for the Anode Nose Cone and Chamber Wall

The temperature results for the back plate of the thruster can be seen in Figure 49. The

material is anodized aluminum with an emissivity of 0.943.
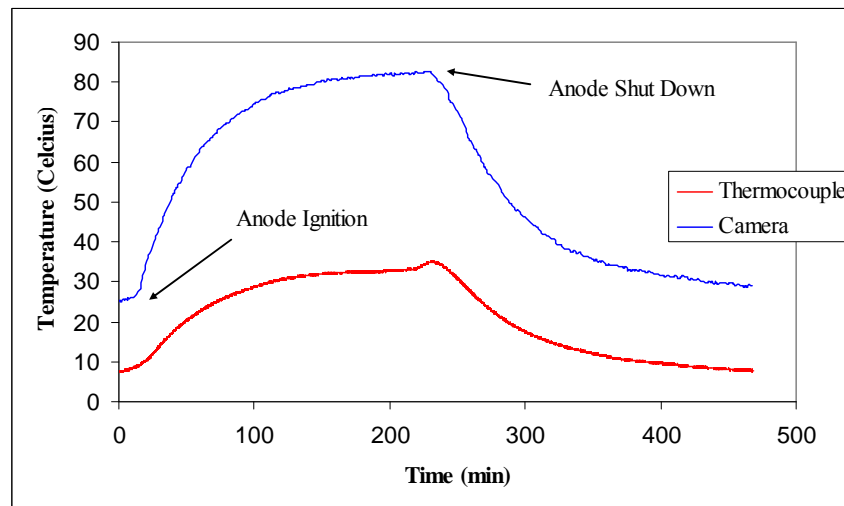
Figure 49. Temperature Profile for the Anodized Aluminum Back Plate

Heat conducts from the anode and the magnets to the anodized aluminum, and causes the

temperature to increase. The temperature decreases during anode shut down.

50

Camera Corrections

Several discrepancies exist between the thermocouple and camera data, shown in the previous figures. Emissivity is not just a material property, but is also a function of the surface finish, wavelength, and direction. The experimentally determined emissivity only takes into account temperature, leading to the differences between the thermocouple and camera data. One way to correct the errors is to adjust the emissivity in ThermaCAM Researcher to match the thermocouple data. Due to the already high emissivities of the alumina, boron nitride, and anodized aluminum, this adjusted emissivity method does not work. The emissivity becomes greater than one, which is blackbody radiation and does not represent a real surface. The adjustment of emissivity works for the stainless steel sections; however, the data does not match due to only taking into account an average temperature emissivity. To account for all of the emissivity errors, the linear trend between the thermocouple and camera data corrects the temperatures. Equation (25) illustrates how to correct the temperature from the trendlines of the temperature differences between the thermocouple and camera.

$$T_{corrected} = T_{camera}(1 - \text{slope}) - \text{intercept} \qquad (25)$$

$T_{corrected}$ is the new temperature, T_{camera} is the temperature from the camera, *slope* is the slope of the trendline, and *intercept* is the y intercept of the trendline. Figure 50 illustrates the temperature differences for the steel section of the cathode, and the temperature differences for the stainless steel side of the thruster can be seen in Figure 51. The R^2 value, known as the coefficient of determination, is an indicator of how well the trendline corresponds to the actual data. Equation (26) shows the coefficient of determination

51

$$R^2 = \frac{\left(\sum_{i=1}^{n}(x_i - \overline{x})(y_i - \overline{y})\right)^2}{\sum_{i=1}^{n}(x_i - \overline{x})^2 \sum_{i=1}^{n}(y_i - \overline{y})^2} \tag{26}$$

where x_i is the x data, y_i is the y data, $\overline{x}$ is the average x data, $\overline{y}$ is the average y data,

and n is the number of samples. It ranges between zero and one, and represents how well

the linear trend represents the data.[35] Since the value is close to one, the linear trend is

reliable.
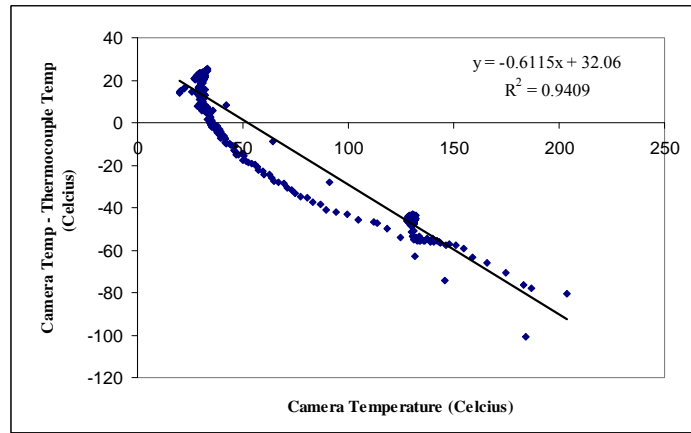
Figure 50. Temperature Differences for the Steel Portion of the Cathode
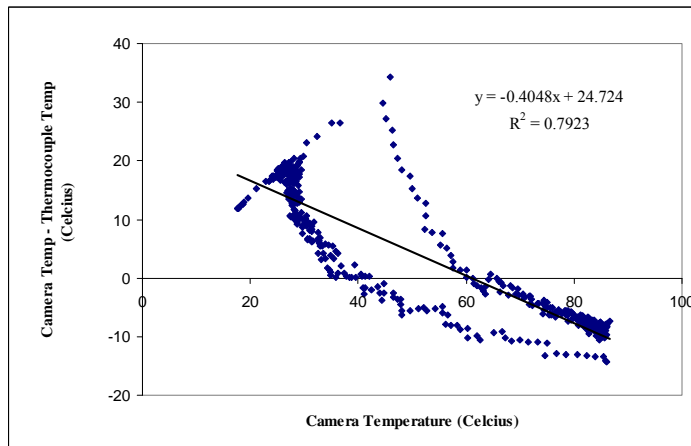
Figure 51. Temperature Differences for the Steel Side of the Thruster

Figure 52 illustrates the corrected camera temperatures for the steel section of the cathode and for the side of the thruster.
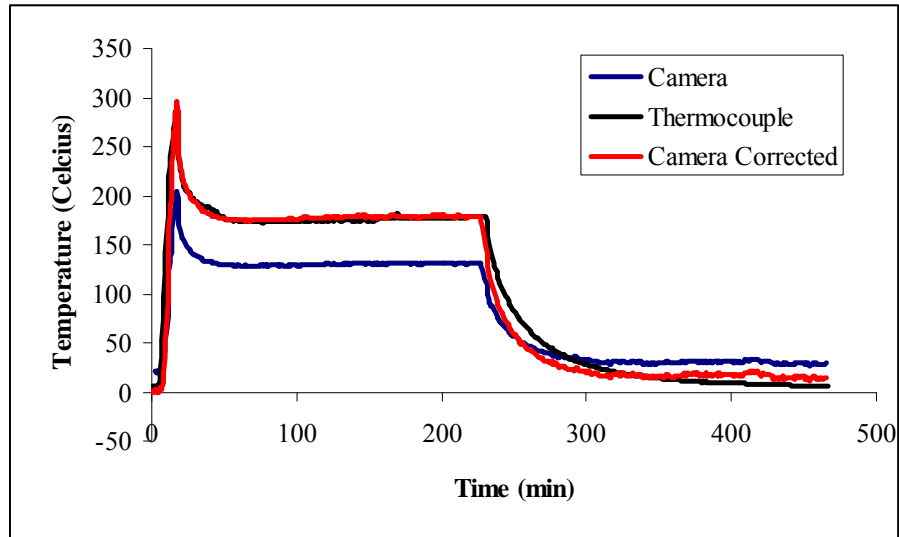
Figure 52. Corrected Camera Temperatures for the Stainless Steel Portion of the Cathode
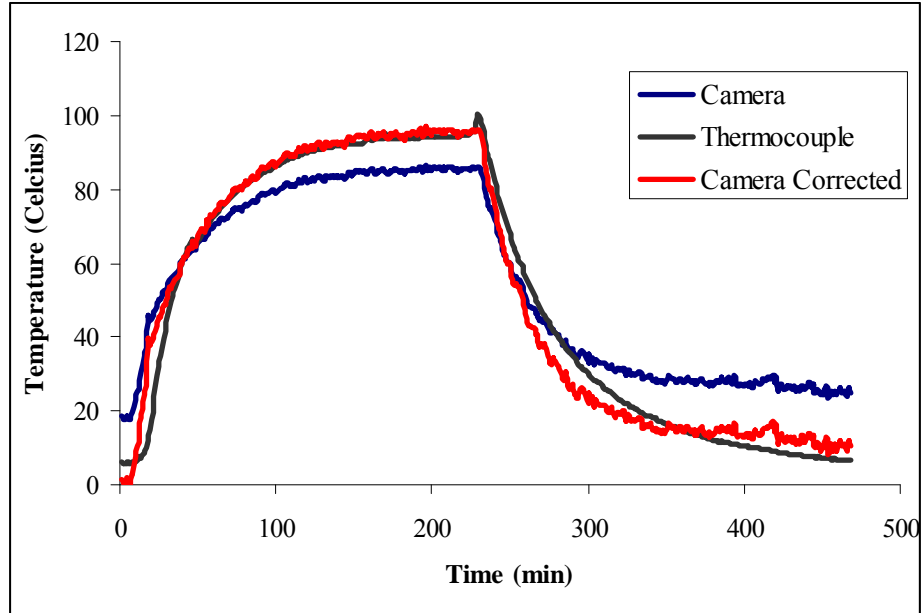
Figure 53. Corrected Camera Temperatures for the Stainless Steel Side of the Thruster

Both stainless steel sections exhibit the same emissivity errors. They also exhibit some new issues at low temperatures. At low temperatures, the camera shows a different

temperature reading than the thermocouple. This is likely due to the low conductivity of the stainless steel and the insulating properties of the ceramic that connect the thermocouple to the surface of the thruster. As the temperature decreases, the insulator covering the thermocouple blocks any radiation cooling and heat can only conduct away from the thermocouple. This insulating condition over the thermocouple could explain the lag in the thermocouple temperature measurements as compared to the camera results as the thruster cools. At some point in the temperature decrease, the camera's temperature becomes greater than the thermocouple's temperature. At this point, the temperature dependence of the emissivity is most pronounced. With the lower emissivities of steel, small changes at these low temperatures can affect the results significantly. The camera values have been corrected using an average emissivity over the entire temperature range introducing some variance in this portion of the data. The temperature of the thermocouple also lags behind the camera temperature during the heating up process due to the ceramic insulator.

Figure 54 displays the temperature differences between the camera and thermocouple for the boron nitride front plate. The corrected camera temperature due to emissivity errors for the boron nitride front plate can be seen in Figure 55. Figure 56 illustrates the temperature differences, and its linear trend for the anodized alumina back plate of the thruster. The anodized aluminum exhibits the strongest linear trend. The corrected camera temperature for the anodized aluminum can be seen in Figure 57. Once again, emissivity errors cause the temperature differences between the original camera measurement and the thermocouple. The temperature corrections for the boron nitride

front plate and the anodized aluminum do not exhibit the same trends as the stainless steel due to the smaller variance in emissivity as a function of temperature.
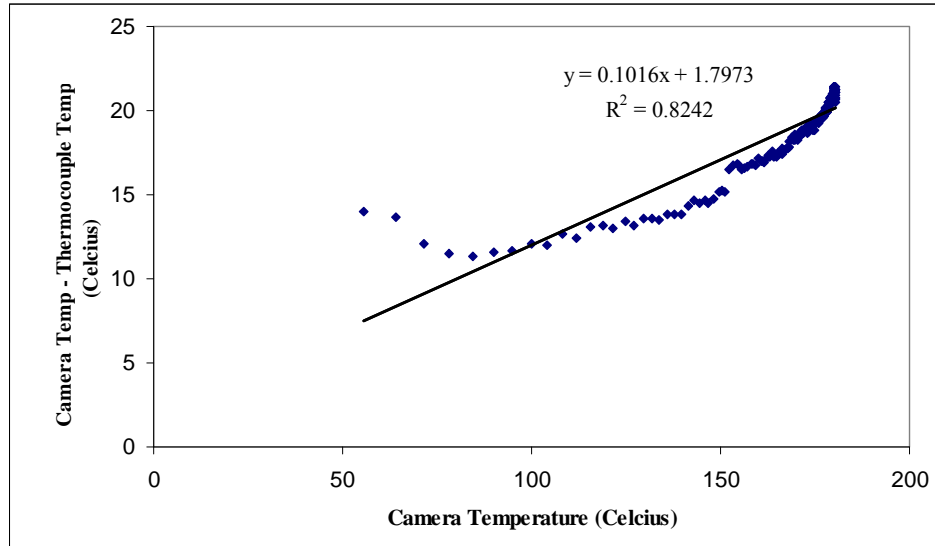
Figure 54. Boron Nitride Front Plate Temperature Differences
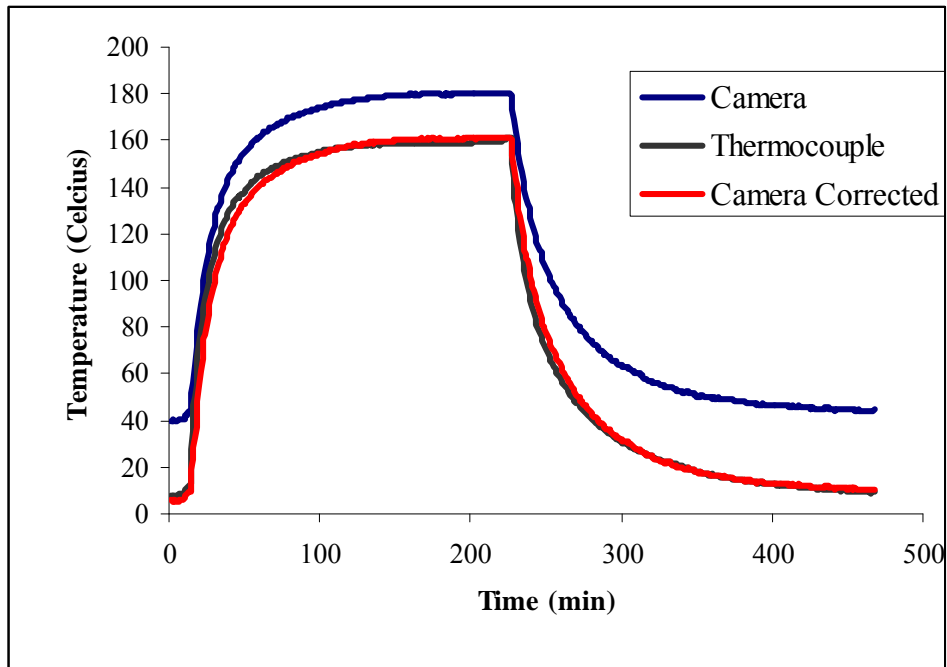
Figure 55. Corrected Camera Temperature for the Boron Nitride Front Plate
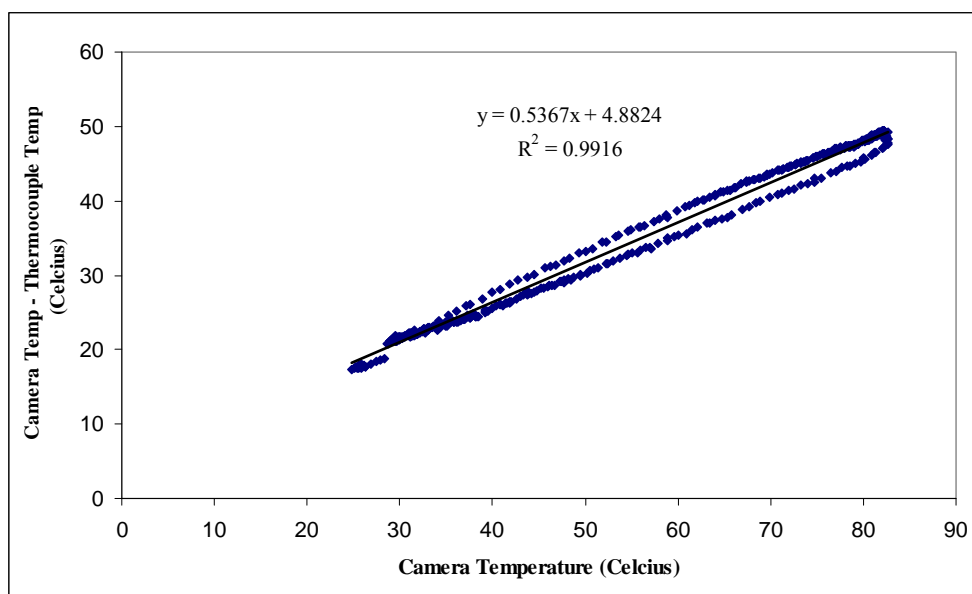
Figure 56. Anodized Aluminum Temperature Differences

The line equation shown on the graph is:
$$y = 0.5367x + 4.8824$$
$$R^2 = 0.9916$$
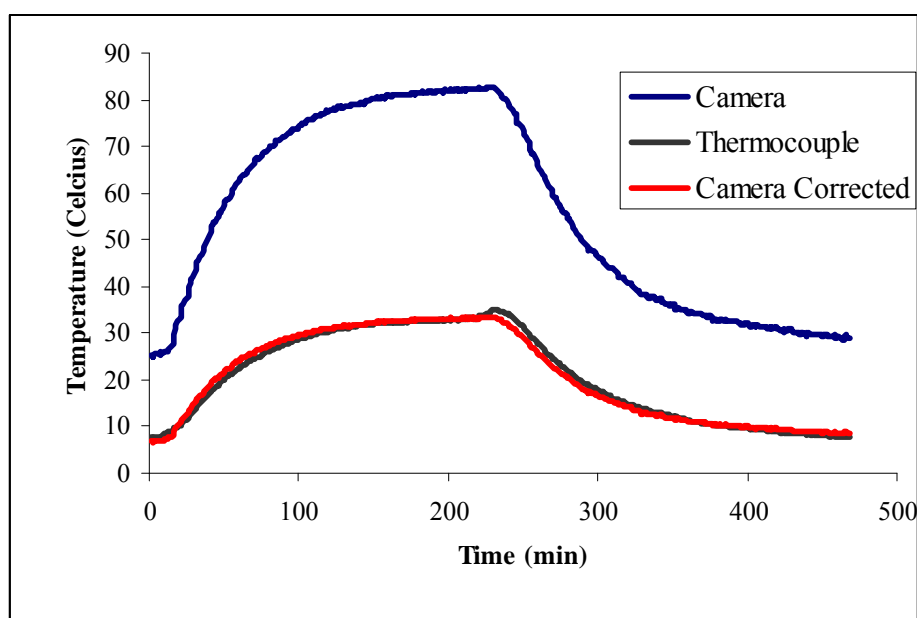
Figure 57. Corrected Camera Temperature for the Anodized Aluminum Back Plate

As discussed previously, the results of the alumina section of the cathode are not likely only due to emissivity errors. Figure 58 shows the corrected camera data for the alumina portion of the cathode using the boron nitride correction factors.
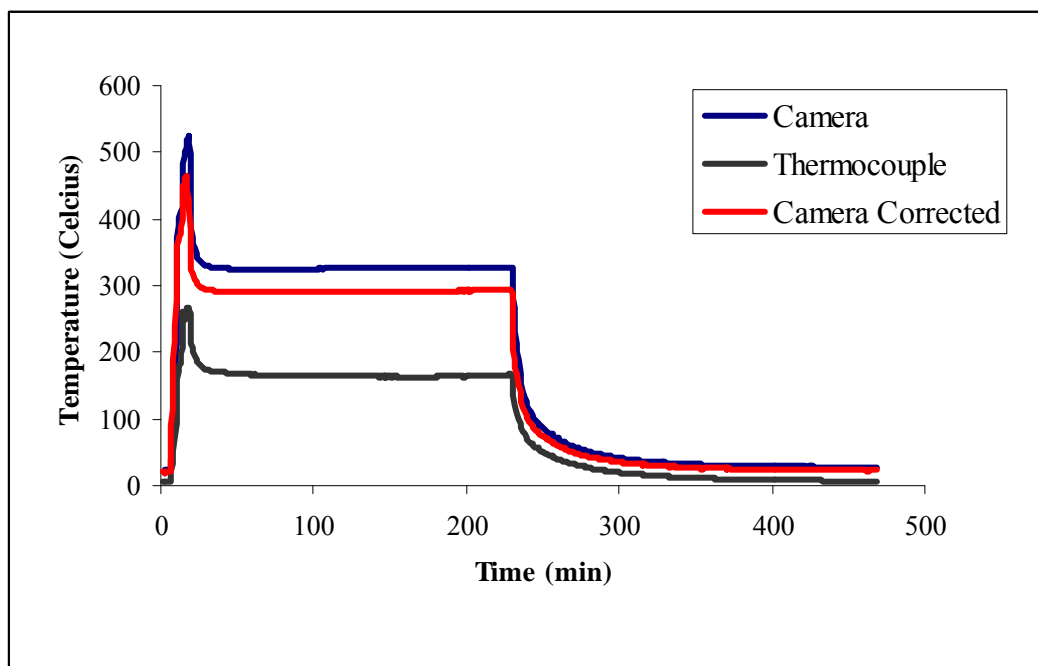
Figure 58. Corrected Camera Data for Alumina

The boron nitride correction factor provides a reasonable thermocouple reading for a

material with a similar emissivity. Also, both boron nitride and alumina are ceramics.

The large temperature difference is due to the lack of surface contact between the

alumina surface and the thermocouple, causing the thermocouple to read lower than

expected. The slope and y intercept for the camera correction equations can be seen in

Table 10.

Table 10: Slope and Intercept Data for Camera Correction

Material	Slope	y Intercept (°C)
Alumina	0.1016	1.7973
Stainless Steel Cathode	-0.6115	32.0605
Stainless Steel Side	-0.4048	24.7241
Boron Nitride	0.1016	1.7973
Anodized Aluminum	0.5367	4.8824

Heating and Cooling Rates

Along with temperature profiles, heating and cooling rates for the cathode and anode nose cone were analyzed using the ThermaCAM software. The heating rates for the three sections can be seen in Figure 59.
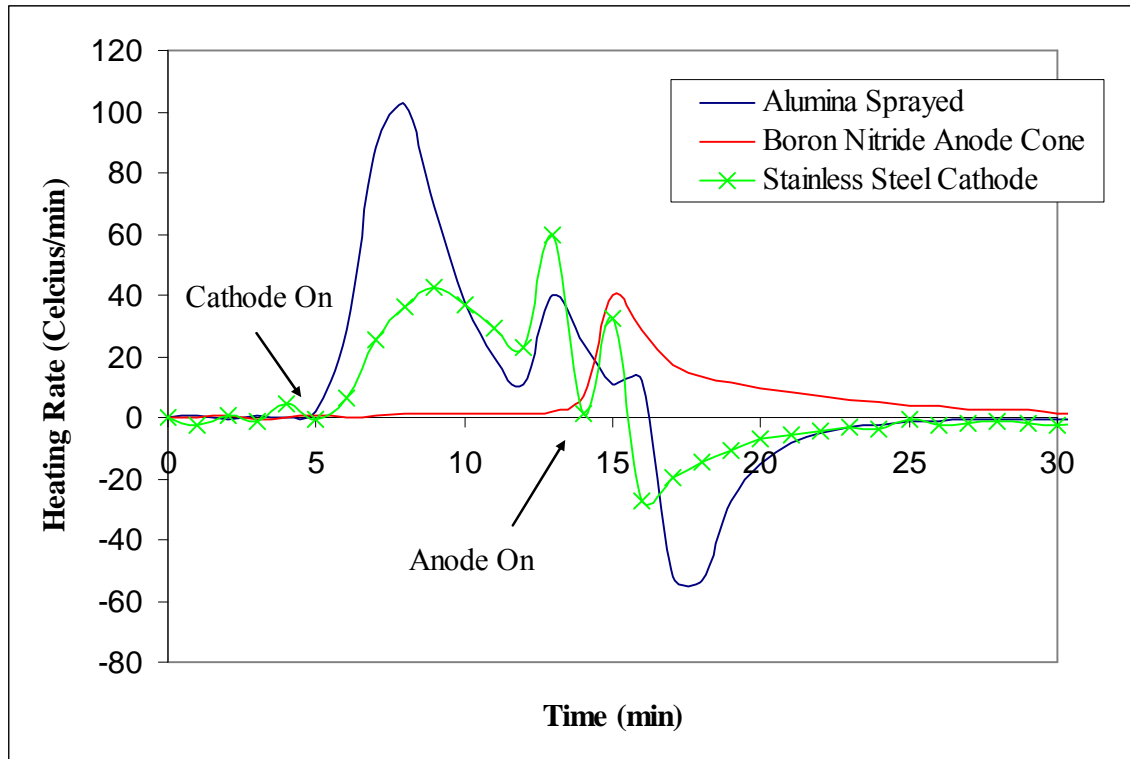
Figure 59. Heating Rates for the Cathode and Anode Nose Cone

During warm up of the cathode, for both the stainless steel and alumina portions of the cathode, the heating rate dramatically increases. The max heating rate for the alumina section is 102 °C/min and 43 °C/min for the steel section. Both sections cool down when the cathode heater current is off and reach a steady state heating at 30 min after start up. The steady state heating rate for the cathode is less than 1 °C/min for the cathode. The anode nose cone heats up during anode ignition to a maximum of 40 °C/min. It reaches steady state heating 17 minutes after anode ignition.

58

The cooling rates for the cathode and the anode nose cone can be seen in Figure 60. The boron nitride anode nose cone cools off after the anode is shut down, with a maximum cooling rate of 17 °C/min.
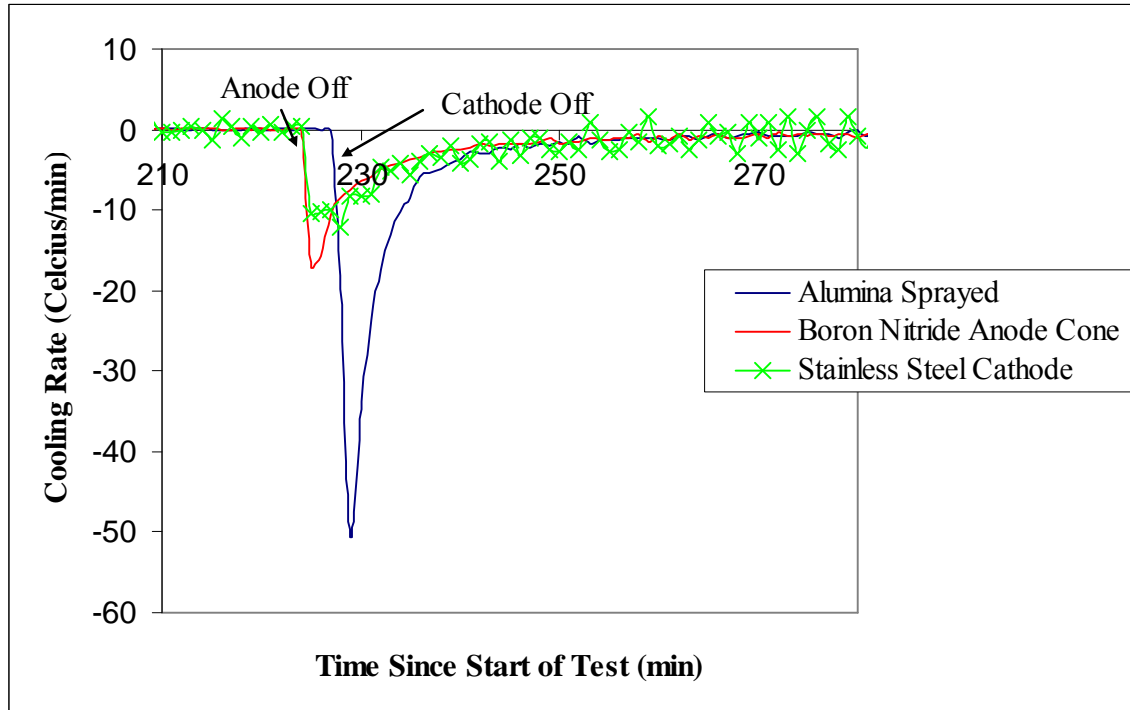
Figure 60. Cathode and Anode Nose Cone Cooling Rates

It reaches a cooling rate of less than 1 °C/min 35 minutes after anode shut down. The cathode also decreases in temperature at shut down. The maximum cooling rate for the alumina section is 50 °C/min and 10 °C/min for the steel section. Each section reaches a steady state cooling rate 35 minutes after cathode shut down.

Thruster Steady State

The steady state images were analyzed using a Matlab code. It combines all of the material emissivities, and corrects the camera temperatures to match the

thermocouple temperatures. Combining Equation (22) with the Stefan-Boltman equation yields the following equation.

$$T_{camera}^4 = \varepsilon\tau T_{obj}^4 + (1-\varepsilon)\tau T_{refl}^4 + (1-\tau)T_{atm}^4 \tag{27}$$

T_{camera} is the original temperature from the camera with an emissivity of one, ε is the emissivity of the object, τ is the atmospheric transmissivity, T_{obj} is the temperature of the object, T_{refl} is the reflected temperature from the vacuum chamber wall, and T_{atm} is the atmospheric temperature. Since the camera is close to the chamber window, the atmospheric transmission is one. Solving for the object temperature yields the equation needed for emissivity changes.

$$T_{obj}^4 = \frac{1}{\varepsilon}T_{camera}^4 - \left(\frac{1-\varepsilon}{\varepsilon}\right)T_{refl}^4 \tag{28}$$

Figure 61 reveals the combined emissivity, steady state image before the camera correction. This image shows the hot section being the alumina sprayed portion of the cathode. It also shows the interaction of the plasma flow with the lower side of the stainless steel section of the cathode. The exit flow causes the lower portion of the cathode to be at a higher temperature than the upper section of the cathode. Figure 62 displays the combined emissivity thermal image with the camera correction the stainless steel, boron nitride, and anodized aluminum. The alumina section is not corrected. Looking at the upper side of the cathode, Figure 62 does not show a smooth transition from the alumina section to the steel section. The alumina section corrected with the boron nitride correction factors can be seen in Figure 63. This image shows a smoother transition from the alumina section of the cathode to the steel section.
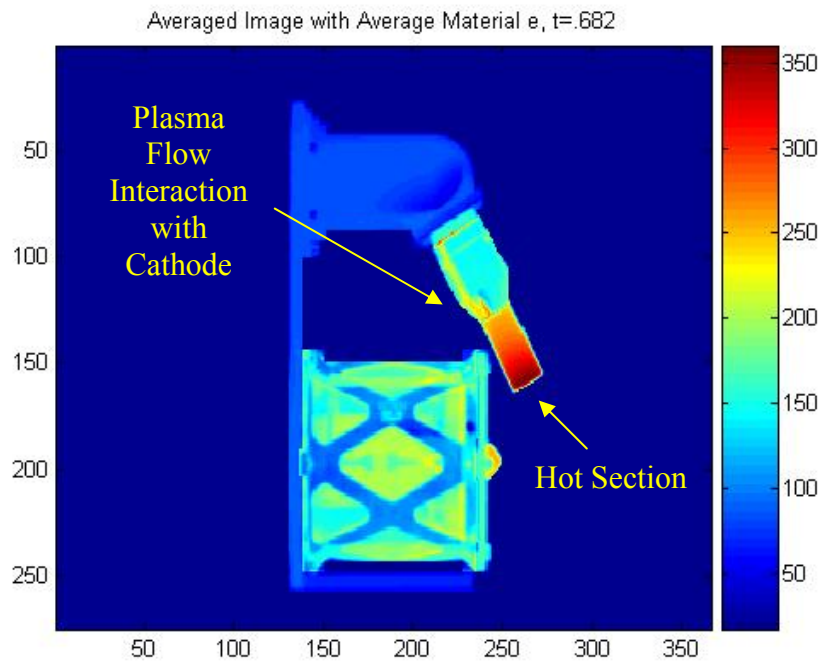
Figure 61. Combined Emissivity Image without Camera Correction
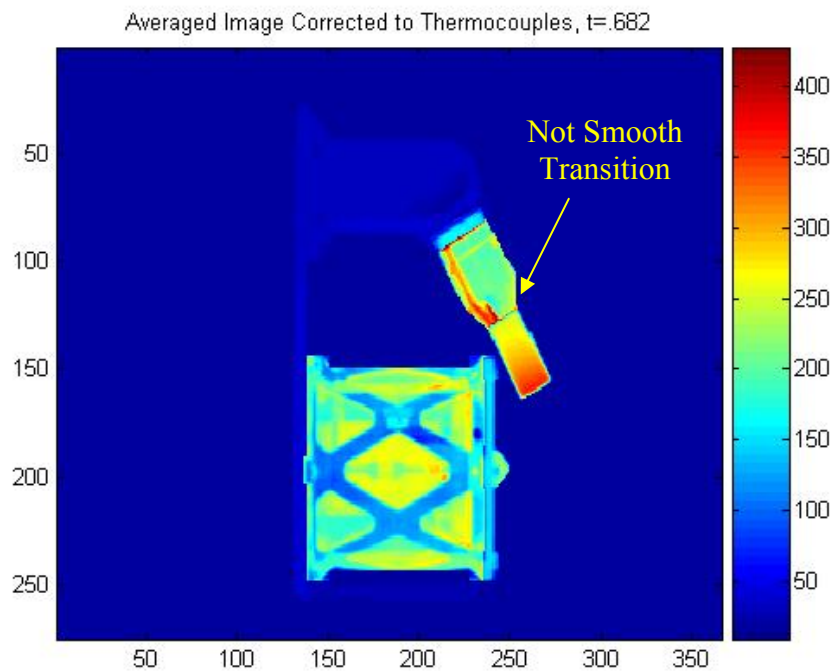
Figure 62. Combined Emissivity Image without the Alumina Camera Correction
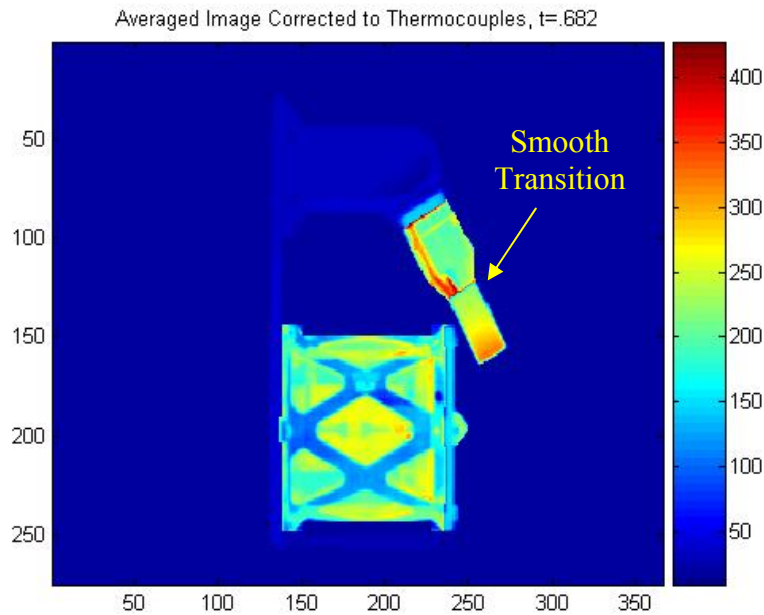
Figure 63. Combined Emissivity Image with Alumina Section Corrected as Boron

Nitride

Figure 64 displays a zoomed in section of the cathode, showing the heating interactions

between the flow and the stainless steel section of the cathode.
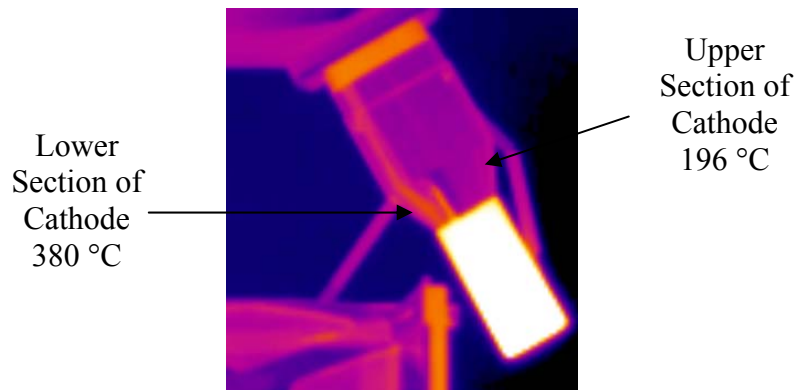
Figure 64. Image of the Exit Flow Interaction with the Cathode

This image appears to be saturated in the alumina section of the cathode because it was

analyzed with the stainless steel emissivity. The lower section of the stainless steel

section of the cathode has a temperature of 380 °C, while the upper section has a

temperature of 196 °C. The xenon flow causes a temperature difference of almost 200 °C.

The following figure shows the rotated steady state image of the Hall thruster.
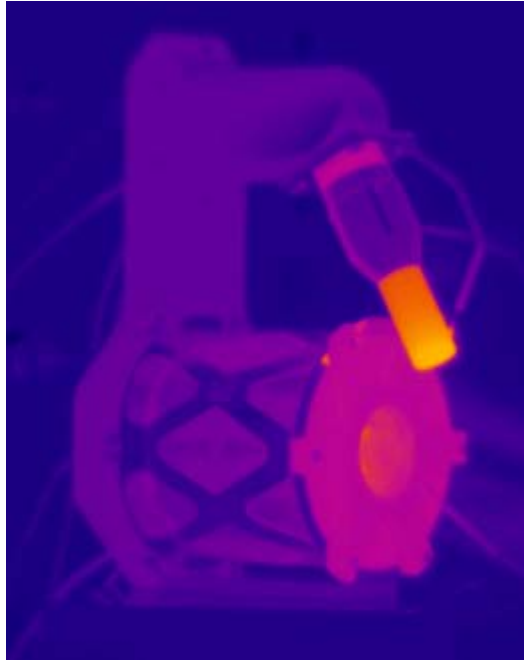
Figure 65. Rotated Steady State Image

The corrected temperature for the alumina cathode tip is 390 °C. The high temperatures of the cathode correspond to the formation of plasma that sustain cathode operation. The temperature of the boron nitride anode nose cone is 217 °C, and the temperature of the chamber wall is 211 °C. Further analysis of these two regions can characterize the erosion characteristics of the boron nitride.

Figure 63 also reveals the Hall Effect thruster magnet temperatures. The highest temperature region of the magnet is middle section with a temperature of 202 °C. The temperature increases from 186 °C at the interior region to the middle portion of the magnet. The temperature then decreases to an exterior magnet temperature of 153 °C.

The temperature difference throughout the magnet is likely due to collisions with high-energy ions. This reveals the middle section of the thruster chamber to be the main location of propellant ionization.

View Factor

The steady state alumina portion of the cathode was analyzed with Matlab using a view factor analysis between the cathode and camera pixels. This code can be seen in Appendix F. It starts by reading in the temperature data from an averaged image. To find the location of the cathode, the image requires a 60° rotation. Equation (28) adjusts the material temperature from the camera temperature, due to the change from the camera emissivity. Equation (29) illustrates the view factor used to adjust the cathode intensities.

$$dF_{pixels\ to\ cathode} = \frac{\cos\theta_1 \cos\theta_2}{\pi S^2} dA_{cathode} \tag{29}$$

F is the view factor from the pixel to the cathode, A is the area of the cathode opposite the area of the pixels, θ_1 is the angle between the pixel normal and the line connecting the two areas, θ_2 is the angle between the cathode area normal and the line connecting the two areas, and S is the length of the line connecting the two areas. Figure 8 illustrates these variables. The upper left corner pixel midpoint is the origin of the right-handed coordinate system used for the view factor calculation. This coordinate system locates the x, y, and z positions for the areas and normal vectors. The dot product relationship calculates the angle between the normal vectors and distance line, and it can be seen in Equation (30).

$$\theta = \cos^{-1}(\frac{S \bullet n}{\|S\|\|n\|}) \tag{30}$$

64

n is the normal vector. Equation (31) describes the new camera intensities in terms of the original camera intensities[14].

$$q_i = A_i (J_i - \sum_{j=1}^{N} F_{ij} J_j)$$

(31)

q is the radiation from the camera, A is the area of the pixel, J is the intensity, and F is the view factor from the pixel to cathode. This leads to a matrix of pixel equations of known radiation and unknown intensities. It is solved for the unknown intensities using Matlab. Equation (11) defines the relationship used to solve for the temperatures from the calculated intensities.

The temperatures, in °C, of the alumina portion of the cathode before the view factor analysis can be seen in Figure 66. The maximum temperature at the cathode tip is 400 °C. Figure 67 displays the temperature of the alumina cathode section after view factor analysis. It too has a maximum temperature of 400 °C. The average temperature difference between the two figures is 0.0174 °C. Since the average temperature difference is less than a degree, the view factor analysis for this experiment is not required. Equation (29) illustrates the reasoning for this conclusion. The distance between the pixels and cathode is several orders of magnitude greater than that of the cathode area. The squared distance value creates even more of a discrepancy between the numerator and denominator, leading to an average view factor of 1.6887×10^{-7}.
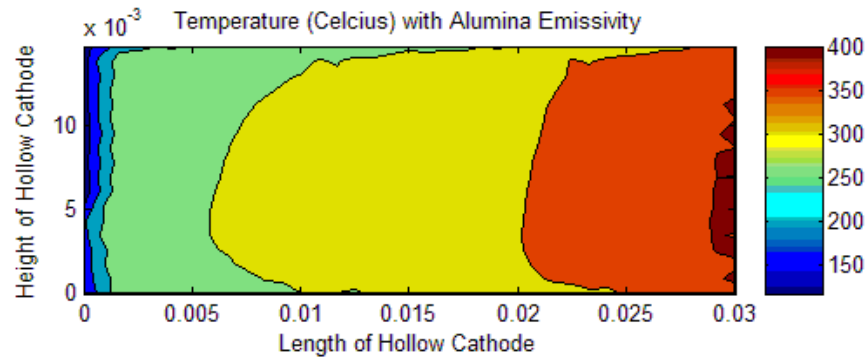
Figure 66. Temperature of Alumina Section of Cathode before View Factor Analysis
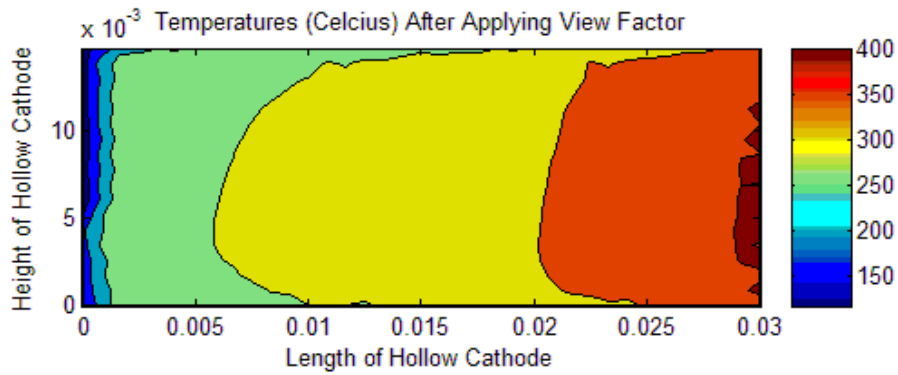
Figure 67. Temperature of Alumina Section of Cathode after View Factor Analysis

The alumina section of the cathode after view factor analysis with the camera correction

for boron nitride can be seen in Figure 68.
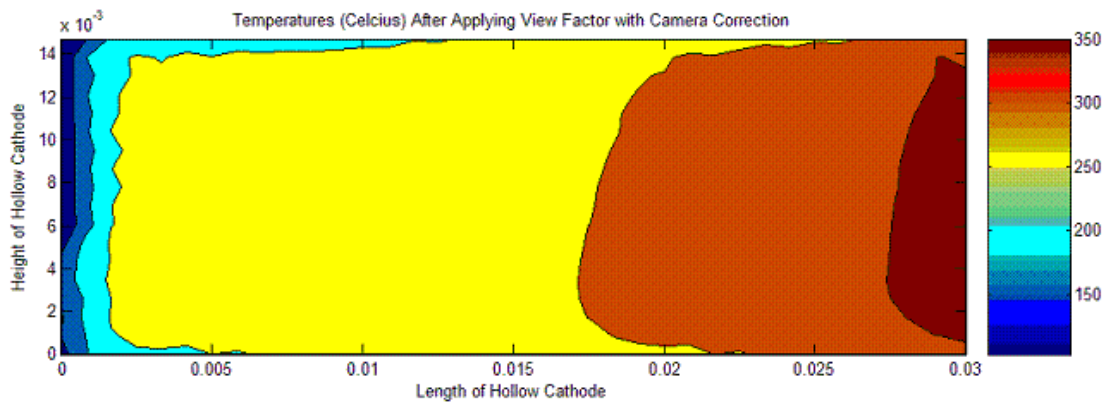
Figure 68. Temperature of Alumina Section of Cathode with Camera Correction

The camera correction changes the maximum temperature from 400 °C to 350 °C.

66

The three previous figures reveal an emissivity dependence on emitted direction. Energy conducted across any cylindrical surface is constant in the radial direction, causing temperature to be constant at a specific radius.[14] The previous figures show less heat being emitted at higher viewing angles of the cathode, and therefore it is not at a constant temperature. Figure 69 illustrates the directional dependence of emissivity for pure titanium. The wavelength of 8.2 micrometers is within the infrared camera's measurement capabilities, and demonstrates how emissivity can increase at higher viewing angles. The alumina section of the cathode also follows this trend. The emissivity increases as the viewing angle increases, leading to smaller temperatures at the higher viewing angle.
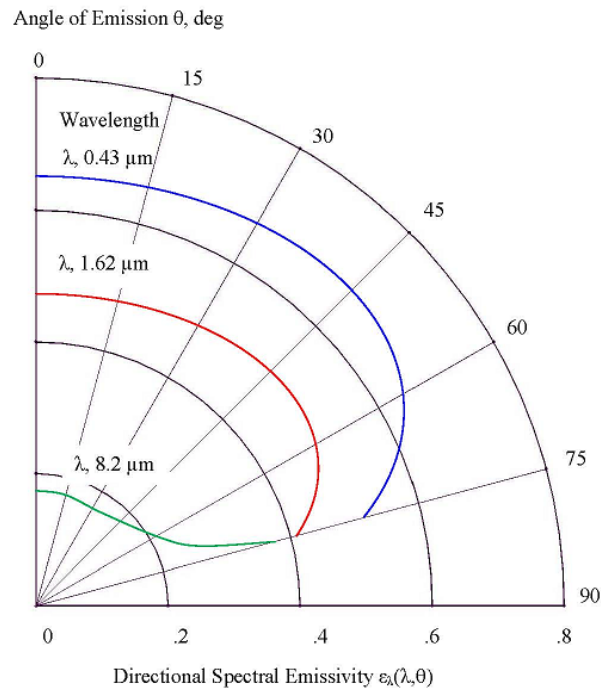
Figure 69. Directional Spectral Emissivity of Pure Titanium[13]

V. Conclusions and Recommendations

Chapter Overview

The objectives of this research were to experimentally determine emissivities, to set up and operate a Hall Effect thruster, and to develop a method to map surface temperature of complex geometries. This chapter reviews the conclusions reached through this research. It also covers recommendations for future research.

Conclusions of Research

Thruster temperature is an important factor affecting thruster design and lifetime. Thermal imaging creates a method for fast, qualitative analysis of an operational Hall thruster. The imager provides an entire mapping of thruster temperatures, as opposed to point-to-point measurements with thermocouples. This type of analysis provides important information on magnet, cathode, and anode temperature. These three affect thruster efficiency, erosion, and lifetime. Thermal imaging also makes available a method to analyze plasma interaction with thruster components. Several drawbacks do exist with the use of thermal imaging.

The major problem with thermal imaging is the calculation of a material's emissivity. The temperature averaged experimentally determined emissivities can be seen in Table 11. Emissivity is a function of temperature, wavelength, angle of emission, material, and a material's surface. Infrared imagers only take into account an average emissivity, leading to errors in the thermal image. Table 12 shows the average errors between the camera data and thermocouples. These errors are due to transmissivity, participating media, and emissivity. Emissivity is the largest contributor.

68

Table 11: Temperature Averaged Emissivities

Material	Temperature Averaged Emissivity
Stainless Steel	0.290
Boron Nitride	0.811
Alumina Plasma Sprayed	0.917
Anodized Aluminum	0.943

Table 12: Average Temperature Errors Due to Emissivity

Material	Average Temperature Error (°C)
Steel Section of Cathode	32.2
Steel Side of Thruster	10.1
Anodized Aluminum	34.6
Boron Nitride Front Plate	26.8

Thermocouples play a key role in correcting these errors; however, they cannot cover the entire thruster surface. This is especially true near the anode nose cone due to the plasma that exits the thruster. Analysis of the thruster's temperature profile requires post processing to correct variances measured by thermocouples to better ground the results. Combing the thermocouple data with the camera measurements, provide greater confidence in the temperature measurements.

Heating rates, cooling rates, and steady state temperatures were analyzed to thermally characterize the thruster. Analysis of the heating and cooling rates yielded the following results for the maximum heating and cooling rates.

Table 13: Maximum Heating and Cooling Rates

Material	Heating Rate (°C/min)	Cooling Rate (°C/min)
Alumina Section of Cathode	102	50
Steel Section of Cathode	43	10
Boron Nitride Nose Cone	40	17

The cathode reached steady state operation (less than 1 °C/min) 30 minutes after cathode start up and the nose cone reached steady state 17 minutes after anode ignition. All the sections reached steady state cooling 35 minutes after shut down. Table 14 displays the steady state temperatures for several of the thruster materials.

Table 14: Steady State Temperatures

Location	Steady State Temperature (°C)
Alumina Sprayed Cathode	327
Stainless Steel Cathode	179
Stainless Steel Side of Thruster	96
Boron Nitride Front Plate	161
Anodized Aluminum Back Plate	33

The interior of the magnet reached a maximum temperature of 186 °C, the middle section of the magnet reached a maximum temperature of 202 °C, and the section of the magnet closest to the exit plane reached a maximum temperature of 153 °C. These temperatures are at least 500 °C less than the Curie temperature of iron (770 °C), and are not expected

70

to affect thruster efficiency. Routine operation of the thruster should not reach the Curie temperature of the magnet; however, it could reach the Curie temperature if the chamber wall erodes enough to expose the magnet to the high temperature plasma.

View factors determine the radiation exchange between two surfaces. The infrared camera pixels receive radiation emitted from all the surfaces of the thruster; however, a view factor analysis of the alumina portion of the thruster showed no effect on the temperature profile. The average change in temperature was 0.0174 °C. This is likely due to the distance between the camera and thruster and the small pixel area, resulting in an average view factor of 1.6887×10^{-7}. The low average temperature difference proves view factor adjustments do not improve accuracy for this test configuration.

The thermal analysis also showed an interaction of the xenon exit flow with the thruster cathode. The steady state images showed a temperature difference between the upper and lower section of the stainless steel cathode. The lower section's temperature is 200 °C greater than that of the upper section.

Recommendations for Future Research

Emissivity differences caused the biggest errors between the camera and thermocouple. The experimentally determined emissivities used in this experiment were averaged across a temperature range. Further examination of the thruster's emissivities as a function of wavelength and emitted direction would decrease the need for the large corrections of camera temperatures. Developing more reliable relationships as a function of temperature could also improve the accuracy of this analysis.

71

Future analysis of the plasma flow field should include the area between the thruster and cathode. The interaction in this region could help explain the temperature differences between the upper and lower sections of the cathode. Another explanation for this heating phenomenon is possible plasma interactions within the cathode. Analysis of cathode operations could also clarify the temperature differences.

Appendix A

Reflected Apparent Temperature Procedures

1. Crumble up a large piece of aluminum foil.

2. Uncrumble the aluminum foil and attach it to a piece of cardboard of the same
   size.

3. Put the piece of cardboard in front of the object you want to measure. Make sure
   that the side with the aluminum foil points to the camera.

4. Set the emissivity to 1.

5. Measure the apparent temperature of the aluminum foil and write it down.

Appendix B

Camera Emissivity Test Procedures

1. Select a place to put the sample.

2. Focus and auto-adjust the camera.

3. Determine and set reflected apparent temperature.

4. Set emissivity to 1.

5. Set atmospheric temperature.

6. Set distance parameter.

7. Heat sample.

8. Adjust level and span for best image brightness and contrast.

9. Freeze the image, and write down thermocouple temperature.

Appendix C

ThermaCAM Researcher Emissivity Calculation Procedures

1. Open thermal image from camera.

2. From analysis toolbar, place a spot, line, box, circle or polygon on the object with known temperature.

3. Select emissivity calculation from the right mouse button menu of the area.

4. Enter known temperature into the emissivity calculation dialog box, and click on calculate to view the new emissivity.

5. Click ok to accept and apply the new emissivity to the area.

Appendix D

Viewport Mechanical Drawing

Outside Flange
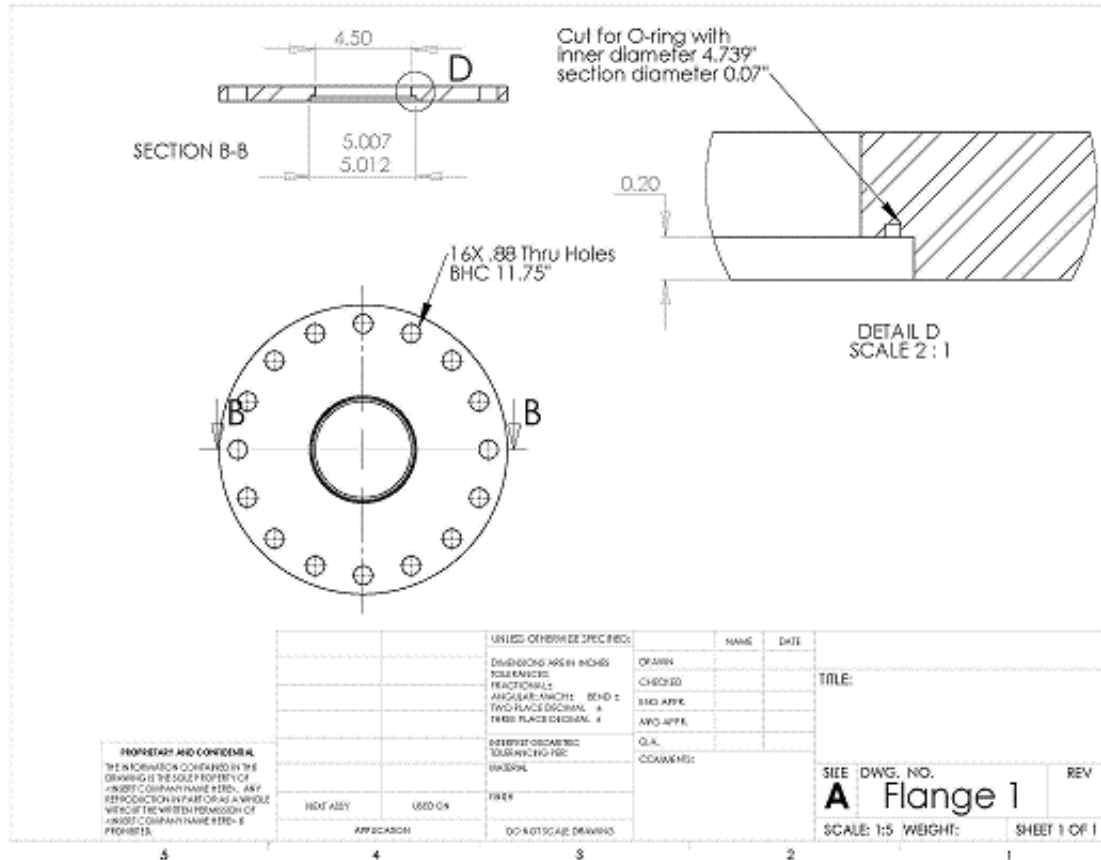
Figure 70. Outer Flange for Window Adapter

Inside Flange
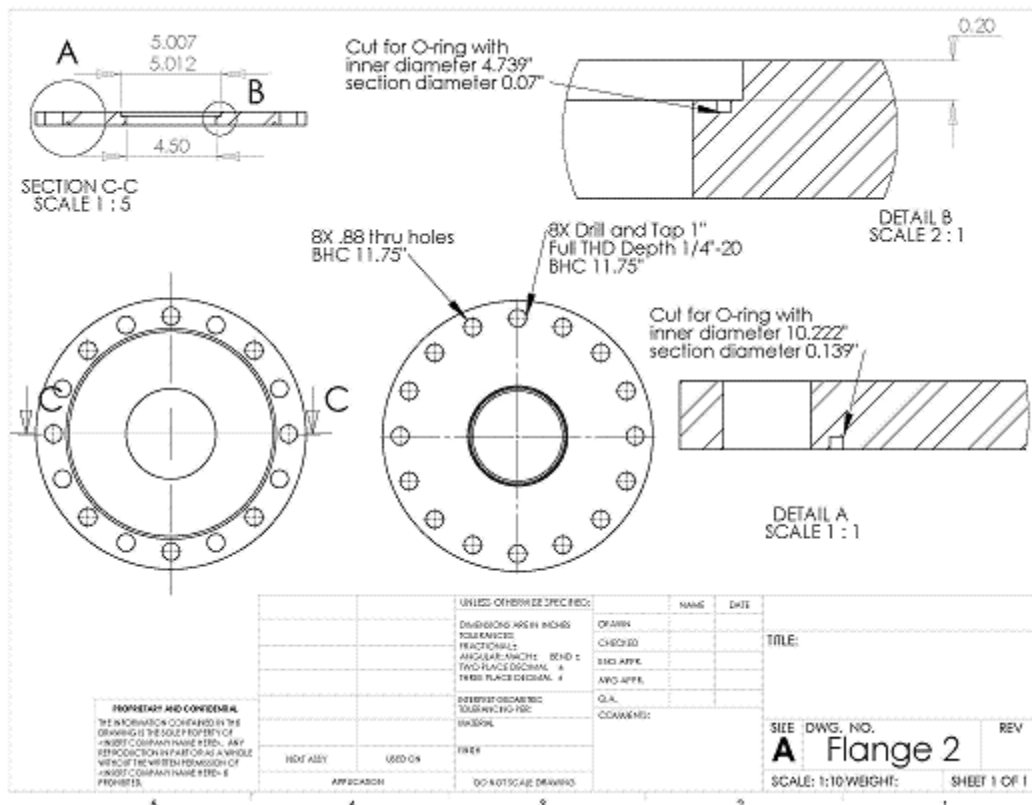
Figure 71. Inner Flange for Window Adapter

Note: Flanges mount together using 8 bolts. Flange 2 drawings calls for ¼-20 bolts, but Flange 1 drawing calls for all 0.88 in through holes. The Flange 1 drawing is incorrect and should have eight thru holes for 0.25 in bolts; however, the flange still seals to the vacuum chamber with this mistake.

Appendix E

Hall Thruster Start Up and Shut Down Procedures

1. Purge propellant tanks with xenon for 155 minutes at a flow rate of 5 sccm.

2. Condition cathode.

   a. Start Manual Thruster Start Up VI.

   b. Turn PPU power on.

   c. Turn PPU cooling fan on.

   d. Set cathode heater to 2 Amps for 90 minutes.

   e. Set cathode heater to 4 Amps for 90 minutes.

   f. Set cathode heater to 6 Amps for 30 minutes.

   g. Set cathode heater to 0 Amps.

Note: Cathode conditioning should be performed following any exposure to atmospheric conditions, defined as 10^{-2} Torr. If the tank pressure increases to above 10^{-4} Torr, but does not reach 10^{-2} Torr, reconditioning the cathode only requires 2 Amps to the cathode heater for 30 minutes.

3. Set anode flow rate to 8 sccm.

4. Set cathode flow rate to 0.8 sccm.

5. Heat cathode to 6.5 amps for approximately 4 minutes.

   a. Cathode heater voltage should be 6 V.

6. Set cathode keeper to 0.5 Amps.

   a. Breakdown occurs at 100 V.

   b. If cathode does not breakdown, keeper voltage will read 600 V, repeat Step 6.

7. Set discharge voltage to 250 V.

    a. Visually check for pink glow.

8. Set magnet current to 1.25 Amps.

    a. Visually check for blue glow.

9. Set cathode heater to 0 Amps after two minutes.

10. After completing test, turn off discharge voltage, then magnet current, and finally keeper current.

11. Turn off propellant flow.

Appendix F

View Factor Matlab Code for Alumina Section of Cathode

```
clc;clear all;
load image.mat

% constants needed

r_cathode = .0079375; % radius of cathode in meters
h_pixel = 8.647663532*10^-4; % height of pixel in meters
l_pixel = 8.337958487*10^-4; % length of pixel in meters
Ap = l_pixel*h_pixel;   % area of pixels in meters squared
diam = 2*r_cathode; %cathode diameter;
l_cathode = 0.03175;% 38 * l_pixel;
e_camera = 1; %camera emissivity
e_as = 0.9172; %alumina sprayed emissivity
pi = 2*acos(0);
T_background = 17 + 273.15;

i0 = 391;
j0 = 220;
x0 = j0 * l_pixel;
y0 = i0 * h_pixel;
slope = ((-255)-(-222))/(408-389); %slope of line from pixel data
rotate_angle = pi/3;%-1*atan(slope); %pi / 4;
n_r = 50; % number of rows ~13
n_c = 50; % number of columns ~56
x_res = l_cathode/n_c;
y_res = diam/n_r;
d = 1.1684; % distance from thruster to window

for i = 1:n_c;
    for j = 1:n_r;
        x_new(i,j) = (i - 1) * l_pixel;
        y_new(i,j) = (j - 1) * h_pixel;
        rad = (x_new(i,j)^2 + y_new(i,j)^2)^.5;
        if (rad>0)
            theta_1(i,j) = acos(x_new(i,j)/rad);
        else
            theta_1(i,j) = 0;
        end
        x_act(i,j) = x0 + rad * cos( (theta_1(i,j) - rotate_angle));
        y_act(i,j) = y0 + rad * sin( (theta_1(i,j) - rotate_angle));
        index_i = int16(x_act(i,j)/l_pixel);
        index_j = int16(y_act(i,j)/h_pixel);
        if((index_i>0)&(index_j>0))
            T_old(i,j) = TC_0001(index_i,index_j);
        end
    end
end

y_min = 0.0008338;
```

```
y_max = 0.032;
x_min = 0.0019;
x_max = 0.017;

for i = 1:n_c;
    for j = 1:n_r;
        index_i = int16(x_act(i,j)/l_pixel);
        index_j = int16(y_act(i,j)/h_pixel);
        if((index_i>0)&(index_j>0))
            if((x_new(i,j)>x_min)&(x_new(i,j)<x_max)&(y_new(i,j)>y_min)&(y_new(i,j)<y_max))
            del_x = x_act(i,j) - double(index_i) * l_pixel;
            del_y = y_act(i,j) - double(index_j) * h_pixel;
            Tijh=(TC_0001(index_i,index_j+1)-
TC_0001(index_i,index_j))*(del_y/h_pixel)+TC_0001(index_i,index_j);
            Tihjh=(TC_0001(index_i+1,index_j+1)-
TC_0001(index_i+1,index_j))*(del_y/h_pixel)+TC_0001(index_i+1,index_j);
            T(i,j) = (Tihjh-Tijh)*(del_x/l_pixel)+Tijh;
            else
                T(i,j) = 0;
            end
        end
    end
end
for i = 1:n_c;
    x_new_vec(i)=x_new(i,1);
    x_act_vec(i)=x_act(i,1);
end
for i = 1:n_r;
    y_new_vec(i)=y_new(1,i);
    y_act_vec(i)=y_act(1,i);
end

figure(1)
subplot(2,1,1)
contourf(x_act_vec,y_act(1,n_r)-y_act_vec,T_old)
colorbar
%contourcmap([200:10:700],'colorbar','on','location','vertical');
title('Temperature (Kelvin) After Rotation')
xlabel('Length of Hollow Cathode')
ylabel('Height of Hollow Cathode')
subplot(2,1,2)
imagesc(T_old)
colorbar
%contourcmap([200:10:700],'colorbar','on','location','vertical');
title('Temperatures (Kelvin) of Pixels')

figure(2)
subplot(2,1,1)
contourf(x_new_vec,y_new(1,n_r)-y_new_vec,T)
% contourcmap([300:50:650],'colorbar','on','location','vertical');
colorbar
title('Averaged Temperature (Kelvin) After Rotation')
xlabel('Length of Hollow Cathode')
ylabel('Height of Hollow Cathode')
```

```matlab
subplot(2,1,2)
imagesc(T)
colorbar
%contourcmap([200:10:700],'colorbar','on','location','vertical');
title('Temperatures (Kelvin) of Pixels')

% finds location of cathode in T matrix and dimensions of cathode
row_upper = 4;
row_lower = 21;
column_left = 2;
column_right = 38;
for i = row_upper:row_lower;
    for j = column_left:column_right;
        Tcathode(i-3,j-1) = T(i,j);
    end
end

[height_cathode,length_cathode] = size(Tcathode);
for i = 1:height_cathode;
    y_cathode(i) = (i-1)*h_pixel;
end
for i = 1:length_cathode;
    x_cathode(i) = (i-1)*l_pixel;
end

%temperature of pixels with new emissivity
for i=1:height_cathode;
    for j=1:length_cathode;
        Tcathode_new(i,j) = (1/e_as)*(Tcathode(i,j)^4-(1-e_as)*T_background^4)^(1/4);
    end
end

figure(3)
subplot(2,1,1)
contourf(x_cathode,y_cathode(1,height_cathode)-y_cathode,Tcathode)
colorbar
%contourcmap([200:10:700],'colorbar','on','location','vertical');
title('Temperature (Kelvin) with Camera Emissivity')
xlabel('Length of Hollow Cathode')
ylabel('Height of Hollow Cathode')
subplot(2,1,2)
imagesc(Tcathode)
colorbar
%contourcmap([200:10:700],'colorbar','on','location','vertical');
title('Temperatures (Kelvin) of Pixels e = 1')


% x,y,z locations of centerline of cathode
for i=1:height_cathode;
    for j=1:length_cathode;
        m=j+(i-1)*length_cathode;
        xcl(m,1) = (j-1)*l_pixel;
        ycl(m,1) = -height_cathode*h_pixel/2 + 0.5*h_pixel;
        zcl(m,1) = d;
```

82

```matlab
        end
    end
    % x,y and z location of pixels and cathode
    for i=1:height_cathode;
        for j=1:length_cathode;
            m=j+(i-1)*length_cathode;
            %pixel locations
            x1(m,1) = (j-1)*l_pixel;
            y1(m,1) = (1-i)*h_pixel;
            z1(m,1) = 0;
            %cathode location
            x2(m,1) = (j-1)*l_pixel;
            y2(m,1) = (1-i)*h_pixel;
            z2(m,1) = d-((height_cathode*h_pixel/2)^2-(y2(m,1)-ycl(m,1))^2)^.5;
        end
    end

    % area of cathode mapped onto pixels
    for i=1:height_cathode;
        for j=1:length_cathode;
            m=j+(i-1)*length_cathode;
            psi = acos((y2(m,1)-ycl(m,1))/(height_cathode*h_pixel/2));
            theta = pi/2 - psi;
            Ac(m,1) = Ap/cos(theta);
        end
    end

    % line and distance between each cathode area and pixel area
    for k=1:height_cathode*length_cathode;
        for i=1:height_cathode;
            for j=1:length_cathode;
                m=j+(i-1)*length_cathode;
                Ax(m,k) = x2(m,1)-x1(k,1);
                Ay(m,k) = y2(m,1)-y1(k,1);
                Az(m,k) = z2(m,1)-z1(k,1);
                A_length(m,k) = ((Ax(m,k))^2 + (Ay(m,k))^2 + (Az(m,k))^2)^.5;
            end
        end
    end

    % normals to pixel and cathode surfaces
    for i=1:height_cathode;
        for j=1:length_cathode;
            m=j+(i-1)*length_cathode;
            n1x(m,1) = 0;
            n1y(m,1) = 0;
            n1z(m,1) = 1;
            n1_length(m,1) = (n1x(m,1)^2+n1y(m,1)^2+n1z(m,1)^2)^.5;
            n2x(m,1) = x2(m,1)-xcl(m,1);
            n2y(m,1) = y2(m,1)-ycl(m,1);
            n2z(m,1) = z2(m,1)-zcl(m,1);
            n2_length(m,1) = (n2x(m,1)^2+n2y(m,1)^2+n2z(m,1)^2)^.5;
        end
    end
```

```matlab
% angles between normals and connecting line for view factor
for k=1:height_cathode*length_cathode;
    for i=1:height_cathode;
        for j=1:length_cathode;
            m=j+(i-1)*length_cathode;
            num1(m,k) = Ax(m,k)*n1x(k,1)+Ay(m,k)*n1y(k,1)+Az(m,k)*n1z(k,1);
            den1(m,k) = A_length(m,k)*n1_length(k,1);
            theta1(m,k) = acos(num1(m,k)/den1(m,k));
            num2(m,k) = -(Ax(m,k)*n2x(m,1)+Ay(m,k)*n2y(m,1)+Az(m,k)*n2z(m,1));
            den2(m,k) = A_length(m,k)*n2_length(m,1);
            theta2(m,k) = acos(num2(m,k)/den2(m,k));
        end
    end
end

%setting up C matrix intensities of each pixel in W
sigma = 5.67*10^-8; %stefan-boltzman constant in W/m^2/K^4
for i=1:height_cathode;
    for j=1:length_cathode;
        m=j+(i-1)*length_cathode;
        C(m,1) = e_as*sigma*Ap*(Tcathode_new(i,j))^4;
    end
end

% set up A matric for inversion each cell equals view factor times area of
% pixel
for k=1:height_cathode*length_cathode;
    for i=1:height_cathode;
        for j=1:length_cathode;
            m=j+(i-1)*length_cathode;
            if (k==m)
                A(k,m) = Ap;
            else
                F_view(m,k) = (cos(theta1(m,k))*cos(theta2(m,k))*Ac(m,1)/pi/(A_length(m,k))^2);
                A(m,k) = -F_view(m,k)*Ap;
            end
        end
    end
end

% solve for pixel intensities, [A][X]=[C]
X = inv(A)*C;

for i=1:height_cathode;
    for j=1:length_cathode;
        Intensity(i,j) = X(j+(i-1)*length_cathode,1);
    end
end

for i=1:height_cathode;
    for j=1:length_cathode;
        Temperature(i,j) = (Intensity(i,j)/sigma/e_as)^(1/4);
    end
```

```matlab
end

% temperatue in celcius
Temperature_new = Temperature - 273.15;

figure(4)
subplot(2,1,1)
contourf(x_cathode,y_cathode(1,height_cathode)-y_cathode,Tcathode_new)
colorbar
%contourcmap([300:10:700],'colorbar','on','location','vertical');
title('Temperature (Kelvin) with Alumina Emissivity')
xlabel('Length of Hollow Cathode')
ylabel('Height of Hollow Cathode')
subplot(2,1,2)
imagesc(Tcathode_new)
colorbar
%contourcmap([300:10:700],'colorbar','on','location','vertical');
title('Temperatures (Kelvin) of Pixels, e = 0.9172')

figure(5)
subplot(2,1,1)
contourf(x_cathode,y_cathode(1,height_cathode)-y_cathode,Temperature)
colorbar
%contourcmap([300:10:700],'colorbar','on','location','vertical');
title('Temperatures (Kelvin) After Applying View Factor')
xlabel('Length of Hollow Cathode')
ylabel('Height of Hollow Cathode')
subplot(2,1,2)
imagesc(Temperature)
colorbar
%contourcmap([300:10:700],'colorbar','on','location','vertical');
title('Temperatures (Kelvin) of Pixels, e = 0.9172')

figure(6)
subplot(2,1,1)
contourf(x_cathode,y_cathode(1,height_cathode)-y_cathode,Temperature_new)
colorbar
title('Temperatures (Celcius) After Applying View Factor')
xlabel('Length of Hollow Cathode')
ylabel('Height of Hollow Cathode')
subplot(2,1,2)
imagesc(Temperature)
colorbar
%contourcmap([300:10:700],'colorbar','on','location','vertical');
title('Temperatures of Pixels, e = 0.9172')

figure(7)
subplot(2,1,1)
contourf(x_cathode,y_cathode(1,height_cathode)-y_cathode,Tcathode_new-273.15)
colorbar
%contourcmap([300:10:700],'colorbar','on','location','vertical');
title('Temperature (Celcius) with Alumina Emissivity')
xlabel('Length of Hollow Cathode')
ylabel('Height of Hollow Cathode')
```

```matlab
subplot(2,1,2)
imagesc(Tcathode_new-273.15)
colorbar
%contourcmap([300:10:700],'colorbar','on','location','vertical');
title('Temperatures (Celcius) of Pixels, e = 0.9172')

% camera correction with boron nitride correction factors
slope_bn = 0.1016;
intercept_bn = 1.7973;
Temperature_corrected = Temperature_new*(1 - slope_bn) - intercept_bn;

figure(8)
subplot(2,1,1)
contourf(x_cathode,y_cathode(1,height_cathode)-y_cathode,Temperature_corrected)
colorbar
%contourcmap([300:10:700],'colorbar','on','location','vertical');
title('Temperatures (Celcius) After Applying View Factor with Camera Correction')
xlabel('Length of Hollow Cathode')
ylabel('Height of Hollow Cathode')
subplot(2,1,2)
imagesc(Temperature_corrected)
colorbar
%contourcmap([300:10:700],'colorbar','on','location','vertical');
title('Temperatures (Celcius) of Pixels, e = 0.9172')
```

Bibliography

[1] Jahn, Robert G. *Physics of Electric Propulsion*. New York: McGraw-Hill, Inc., 1968.

[2] Wertz, James R. and Wiley J. Larson. *Space Mission Analysis and Design 3rd Edition*. California: W. J. Larson and Microcosm, Inc., 1999.

[3] European Space Agency. "SMART-1." n. pag. http://www.esa.int/SPECIALS/SMART-1/index.html. 24 September 2007.

[4] National Aeronautics and Space Administration. "TacSat-2." n. pag. http://www.nasa.gov/mission_pages/tacsat-2/main/index.html. 24 September 2007.

[5] Humble, Ronald W., Gary N. Henry and Wiley J. Larson. *Space Propulsion Analysis and Design*. New York: McGraw-Hill, Inc., 1995.

[6] Jiles, David. *Introduction to Magnetism and Magnetic Materials*. New York: Chapman and Hall, 1991.

[7] Kaplan, Herbert. *Practical Applications of Infrared Thermal Sensing and Imaging Equipment Third Edition*. Washington: SPIE, 2007.

[8] Hill, Philip and Carl Peterson. *Mechanics and Thermodynamics of Propulsion*. Massachusetts: Addison-Wesley Publishing Company, 1992.

[9] Sutton, George P. and Oscar Biblarz. *Rocket Propulsion Elements 7th Edition*. New York: John Wiley & Sons, Inc., 2001.

[10] Spores, Ronald A. and Frank S. Gulczinski, III, "Analysis of Hall-Effect Thrusters and Ion Engines for Orbit Transfer Missions," AIAA 1996-2973.

[11] The Internet Encyclopedia of Science. "Hall Effect Thruster." n. pag. http://www.daviddarling.info/encyclopedia/H/Halleffectthruster.html. 5 October 2007.

[12] National Aeronautics and Space Administration. "Hall Thruster Overview." n. pag. http://www.grc.nasa.gov/WWW/hall/overview/overview.htm. 5 October 2007.

[13] Siegel, Robert and John R. Howell. *Thermal Radiation Heat Transfer 3rd Edition*. Washington, DC: Hemisphere Publishing Corporation, 1992.

[14] Incropera, Frank P. and others. *Fundamentals of Heat and Mass Transfer*. New Jersey: John Wiley & Sons, 2007.

[15] McGee, Thomas D. *Principles and Methods of Temperature Measurement*. New York: John Wiley & Sons, 1988.

[16] Bejan, Adrian and Allan D. Kraus. *Heat Transfer Handbook*. California: Wadsworth Publishing Company, 1966.

[17] Holst, Gerald C. *Common Sense Approach To Thermal Imaging*. Florida: JCD Publishing, 2000.

[18] FLIR Systems, ThermaCAM SC640 User's Manual, Pub. No. 1558550, Rev. a201, 16 January 2007.

[19] Liu, Shiquan, and others, "Magnetism of Iron-Containing MCM-41 Spheres," Journal of Magnetism and Magnetic Materials 280 (2004) 31-36.

[20] Yim, John T., Michael Keidar and Iain D. Boyd. "An Investigation of Factors Involved in Hall Thruster Wall Erosion Modeling," AIAA 2006-4657.

[21] Domonkos, Matthew T., Alec D. Gallimore and MichaelJ. Patterson. "Thermographic Investigation of 3.2 mm Diameter Orificed Hollow Cathodes," AIAA 1998-3793.

[22] Van Noord, Jonathan L. Hani Kamhawi and Heather K. McEwen. "Characterization of a High Current, Long Life Hollow Cathode," NASA TM-214095, 2006.

[23] Xin, Yu. "Infrared Thermal Imaging Technique: Advances and Prospects, NAIC-ID(RS)T-0402-95.

[24] Beattie, Alan G. and Mark Rumsey. "Non-Destructive Evaluation of Wind Turbine Blades Using an Infrared Camera," AIAA 1999-0046.

[25] Ajdari, E., E. Gutmark, T.P. Parr, K.J. Wilson, and K.C. Schadow. "Thermal Imaging of Afterburning Plumes," AIAA-89-0062.

[26] Horvath, Thomas, Scott Berry, Stephen Alter, Robert Blanchard, Richard Schwartz, Martin Ross and Steve Tack, "Shuttle Entry Imaging Using Infrared Thermography," AIAA-2007-4267.

[27] Mazouffre, S., P. Echegut and M. Dudeck. "A Calibrated Imaging Study on the Steady State Thermal Behavior of Hall Effect Thrusters." *Plasma Sources Science and Technology*, 16:13-22 (2007).

[28] Matlock, Taylor S., William A. Hargus and C. William Larson. "Thermographic Characterization and Comparison of 200W and 600W Hall Thrusters," *Proceedings of the 43rd AIAA/ASME/SAE/ASEE Joint Propulsion Conference*. Ohio, 2007.

[29] Tomaszewski, James W. *Characterization of a Hall Effect Thruster Using Thermal Imaging*. MS Thesis, AFIT/GA/ENY/07-M18. School of Engineering and Management, Air Force Institute of Technology (AU), Wright-Patterson AFB OH, 22 March.

[30] FLIR Systems. "ThermaCAM SC640." n. pag. http://www.flirthermography.com/EMEA/cameras/camera/1080/. 13 October 2007.

[31] Busek Co. Inc., Low Power Nominal Specifications, 2007.

[32] Laser Optex. "Zinc Selenide Optics." n. pag. http://www.laseroptex.com/PRNOznsewindows.asp. 12 January 2008.

[33] FLIR Systems. ThermaCAM Researcher User Manual, Pub. No. 1 558 071, Rev. a196, 21 December 2006.

[34] Busek Co, Inc and AFRL/PRSS, Busek 200 W Hall Thruster Lifetest Test Plan, 5 Nov 2003.

[35] Wackerly, Dennis, William Mendenhall III and Richard Scheaffer. *Mathematical Statistics with Applications*. California: Wadsworth Group, 2002.

REPORT DOCUMENTATION PAGE

The public reporting burden for this collection of information is estimated to average 1 hour per response, including the time for reviewing instructions, searching existing data sources, gathering and maintaining the data needed, and completing and reviewing the collection of information. Send comments regarding this burden estimate or any other aspect of the collection of information, including suggestions for reducing this burden to Department of Defense, Washington Headquarters Services, Directorate for Information Operations and Reports (0704-0188), 1215 Jefferson Davis Highway, Suite 1204, Arlington, VA 22202-4302. Respondents should be aware that notwithstanding any other provision of law, no person shall be subject to an penalty for failing to comply with a collection of information if it does not display a currently valid OMB control number.
PLEASE DO NOT RETURN YOUR FORM TO THE ABOVE ADDRESS.

1. REPORT DATE (DD-MM-YYYY) 27-03-2008	2. REPORT TYPE Master's Thesis	3. DATES COVERED (From – To) March 2007 – March 2008

4. TITLE AND SUBTITLE	5a. CONTRACT NUMBER
THERMAL CHARACTERIZATION OF A HALL EFFECT THRUSTER	5b. GRANT NUMBER
	5c. PROGRAM ELEMENT NUMBER
6. AUTHOR(S) Bohnert, Alex M., Civilian, USAF	5d. PROJECT NUMBER
	5e. TASK NUMBER
	5f. WORK UNIT NUMBER

7. PERFORMING ORGANIZATION NAMES(S) AND ADDRESS(S) Air Force Institute of Technology Graduate School of Engineering and Management (AFIT/EN) 2950 Hobson Way, Building 640 WPAFB OH 45433-8865	8. PERFORMING ORGANIZATION REPORT NUMBER AFIT/GA/ENY/08-M01

9. SPONSORING/MONITORING AGENCY NAME(S) AND ADDRESS(ES) Air Force Research Lab Propulsion Directorate Mr. Michael Huggins 5 Pollux Drive Edwards AFB, CA 93524	10. SPONSOR/MONITOR'S ACRONYM(S)
	11. SPONSOR/MONITOR'S REPORT NUMBER(S)

12. DISTRIBUTION/AVAILABILITY STATEMENT

APPROVED FOR PUBLIC RELEASE; DISTRIBUTION UNLIMITED.

13. SUPPLEMENTARY NOTES

14. ABSTRACT
The thermal characteristics of a Hall thruster directly influence thruster and spacecraft design. High temperatures affect the magnetic coil capabilities and cause higher insulator erosion rates, influencing both thruster performance and lifetime. The Hall thruster transfers heat through both radiation and conduction, and the spacecraft must handle this additional thermal energy. An infrared camera provides a non-intrusive method to analyze the thermal characteristics of an operational Hall thruster. This thesis contains the thermal analysis of a Busek Co. Inc. 200 W Hall thruster, using a FLIR ThermaCAM SC640 infrared camera. The Space Propulsion Analysis and System Simulator Laboratory at the Air Force Institute of Technology on Wright-Patterson Air Force Base provided the location for thruster set up and operation. The infrared camera furnishes the surface temperatures for the entire thruster, and approximates the transient heating behavior during start up, steady state, and shut down. Thermocouples verify and correct the camera data. Experimentally determined emissivities characterize the materials of the thruster. In addition, a view factor analysis between the camera pixels and the alumina sprayed portion of the cathode determines the exchange of radiation between the pixels and cathode surface. This process develops a technique to map surface temperatures of complex geometries with confidence in the actual values. Accurately mapping the surface temperatures of a Hall Effect thruster will improve both thruster efficiency and lifetime, and predict the thruster's thermal load on a satellite.

15. SUBJECT TERMS
Hall Effect Thruster, Hall Thruster, Space Propulsion, Thermal Imaging, Thermal Characterization, Temperature, Space Systems, Emissivity

16. SECURITY CLASSIFICATION OF:			17. LIMITATION OF ABSTRACT	18. NUMBER OF PAGES	19a. NAME OF RESPONSIBLE PERSON Richard D. Branam, Maj, USAF
a. REPORT	b. ABSTRACT	c. THIS PAGE			19b. TELEPHONE NUMBER (Include area code) (937) 255-3636, ext 7485
U	U	U	UU	105	(richard.branam@afit.edu)